Astronomy & Astrophysics manuscript no. 8719
April 28, 2008

The Nature of Mid-Infrared Excesses From Hot Dust Around Sun-like Stars

R. Smith[1,2], M. C. Wyatt[1], and W.R.F. Dent[3]

[1] Institute of Astronomy, University of Cambridge, Madingley Road, Cambridge CB3 0HA, UK
e-mail: rsed@ast.cam.ac.uk

[2] Institute for Astronomy, Royal Observatory Edinburgh, Blackford Hill, Edinburgh EH9 3HJ, UK

[3] U.K. Astronomy Technology Centre, Royal Observatory Edinburgh, Blackford Hill, Edinburgh EH9 3HJ, UK

Accepted : 25th April 2008

ABSTRACT

Aims. Studies of the debris disk phenomenon have shown that most systems are analogous to the Edgeworth-Kuiper Belt (EKB). However a rare subset of sun-like stars possess dust which lies, in contrast, in the terrestrial planet region. In this study we aim to determine how many sources with apparent mid-infrared excess are truly hosts of warm dust, and investigate where the dust in these systems must lie.
Methods. We observed using ground-based mid-infrared imaging with TIMMI2, VISIR and MICHELLE a sample of FGK main sequence stars previously reported to have hot dust. A new modelling approach was developed to determine the constraints that can be set on the radial extent of excess emission in such observations by demonstrating how the detectability of a disk of a given flux as a fraction of the total flux from the system ($F_{\rm disk}/F_{\rm total}$) depends primarily on the ratio of disk radius to PSF width and on the uncertainty on that PSF width.
Results. We confirm the presence of warm dust around three of the candidates; η Corvi, HD145263 and HD202406. For η Corvi modelling constrains the dust to lie in regions smaller than ~3.5 AU. The modelling constrains the dust to regions smaller than 80-100AU for HD145263 and HD202406, with SED fitting suggesting the dust lies at a few tens of AU. Of two alternative models for the η Corvi excess emission, we find that a model with one hot dust component at less than 0.″164 (<3 AU) (combined with the known submm dust population at ~ 150 AU) fits all the data better at the 2.6 σ level than an alternative model with two populations of dust emitting in the mid-infrared: hot dust at less than 0.″19 (< 3.5 AU) and a mid-temperature component at ~ 0.″66 (12 AU). We identify several systems which have a companion (HD65277 and HD79873) or background object (HD53246, HD123356 and HD128400) responsible for their mid-infrared excess, and for three other systems we were able to rule out a point-like mid-infrared source near the star at the level of excess observed in lower resolution observations (HD12039, HD69830 and HD191089).
Conclusions. Hot dust sources are either young and possibly primordial or transitional in their emission, or have relatively small radius steady-state planetesimal belts, or they are old and luminous with transient emission. High resolution imaging can be used to constrain the location of the disk and help to discriminate between different models of disk emission. For some small disks, interferometry is needed to resolve the disk location.

Key words. circumstellar matter – planetary systems: formation

1. Introduction

Analysis of the IRAS database over the last 20 years has shown that there are over 300 main sequence stars that have dust disks around them. This material is thought to be the debris left over at the end of the planet formation process (e.g. Mannings and Barlow 1998). The spectral energy distribution (SED) of this excess in the best studied cases (e.g., Vega, β Pictoris, Fomalhaut, ϵ Eridani) peaks longward of 60μm implying that this dust is cool (<80K), and so resides in Edgeworth-Kuiper belt (EKB)-like regions in the systems. The EKB-like location and analogy is confirmed in the few cases where these disks have been resolved (e.g., Holland et al. 1998, Greaves et al. 2005, see also scattered-light imaging, e.g. Kalas et al. 2007), since the dust is shown to lie >40AU from the stars, and its short lifetime means that it must be continually replenished by the collisional destruction of km-sized planetesimals (Wyatt & Dent 2002). The inner 40AU radius hole is thus thought to arise from clearing by an unseen planetary system, the existence of which is supported by the presence of clumps and asymmetries seen in the structure of the dust rings (e.g., Wyatt et al. 1999; Wyatt 2003). Of the four archetypal objects, only β Pictoris also has (a relatively small amount of) resolved dust in this inner region (Lagage and Pantin 1994, Telesco et al. 2005), thought to be there because this is a young (12Myr, Zuckerman et al.

Send offprint requests to: R. Smith

2001) transitional system in which these regions have yet to be fully cleared by planet formation processes. However Absil et al. (2006) have recently presented interferometric data showing Vega (thought to be around 380-500Myr old, Peterson et al. 2006) is likely to possess extended dust emission within 8AU, and Di Folco et al. (2007) have also recently presented evidence for hot dust around the 10Gyr old τ Ceti.

Zuckerman (2001) noted that out of a large sample of main sequence stars that exhibit excess mid-infrared emission (Mannings and Barlow 1998) half of these showed an excess at 25 μm only. While this seems to suggest a large fraction of systems host warm dust at a few AU, in fact the vast majority of such warm dust systems are around the more luminous A and B stars (see e.g. Rieke et al. (2005), Beichman et al. (2006)), and so despite the fact that the dust is warm, it usually still resides at 10s of AU in regions analogous to the EKB. In contrast hot dust seems to be rare around the less luminous F, G and K-type stars. Four surveys have searched for hot dust around such stars by examining the emission at 25μm above photospheric levels as measured by IRAS (Gaidos 1999), ISO (Laureijs et al. 2002) and Spitzer (Hines et al. 2006; Bryden et al, 2006). All these surveys found evidence for hot dust with fractional luminosity $f = L_{IR}/L_* > 10^{-4}$ in only $2 \pm 2\%$ of stars (for comparison the luminosity of the zodiacal cloud is $10^{-8} - 10^{-7} L_\odot$, Dermott et al. 2002). These systems could represent a departure from the canonical picture that extrasolar debris systems are analogous to our own Kuiper belt, since the temperature of the dust implies that most lies in the region 2-20AU. Thus this dust is predicted to lie at distances from their stars that would be between our asteroid and Kuiper belts, and so in the region where we expect gas giant planets to form - just where we expect no dust. These disks pose several fundamental questions about the outcome of planet formation in these systems. Are these the Kuiper belts of systems in which planet formation failed beyond $\sim$ 10AU (e.g., due to a stellar flyby, Larwood and Kalas 2001, or the rapid dispersal of the protoplanetary gas disk, Hollenbach et al. 2000)? Or are we witnessing the collisional destruction of massive asteroid belts or the sublimation of comets in the middle of fully formed planetary systems? Or dust from a more distant belt trapped in resonance with a giant planet (Moran et al. 2004)? Or perhaps these are systems in a transitional (mid-planet formation) stage (Kenyon & Bromley 2002)?

To begin to tackle these issues, we need to know the true dust distribution in these systems. This can be determined from SED fitting to multi-wavelength infrared photometry, and from constraints provided by resolved imaging. There are several uncertainties regarding these putative disks, in addition to the temperature of the dust emission. Most importantly, the excesses taken from the IRAS database cannot be used at face value. It was noted by Song et al. (2002), who searched the IRAS database for excess emission towards M-type stars, that when searching a large number of stars for excesses close to the detection threshold, a number of false positives must be expected due to noise. Also, there have been a few instances in which the IRAS excess has been shown to be attributed to background objects that fall within the relatively large IRAS beams (>30"). Such objects range from highly reddened carbon stars or Class II YSO's (Lisse et al. 2002), to distant galaxies (Sheret et al. 2004). Another possible source of mid-infrared excess emission is reflection nebulosity (Kalas et al. 2002). Indeed it is now routine for papers discussing the excess sources found by IRAS to address the possibility that some of these are bogus debris disks (Moor et al. 2006, Rhee et al. 2007). Thus it is imperative that we determine if the excesses are real and centred on the stars.

This paper is structured as follows: In §2 the sample selection is described. In §3 the various observational and analysis techniques employed for each instrument are outlined, and in section §4 a new method of placing quantifiable extension limits on unresolved disk images is described. The results, analysis and discussion of individual sources are presented in §5, and the implications of these results discussed in §6. Conclusions are in §7.

2. The Sample

The sample consists of F, G and K stars with IRAS published detections of excess emission at 12 and/or 25 μm. [1] A first-cut was applied to the list of all published detections consisting of the following analysis to determine if the excess identified by IRAS was likely to be real.

For all stars in the sample J, H and K fluxes are obtained from 2MASS and V and B magnitudes from Tycho2. The Michigan Spectral Catalogues or SIMBAD were used to determine the stellar spectral type. This was used to model the photospheric emission based on a Kurucz model atmosphere appropriate to the spectral type and scaled to the K band flux. This allowed determination of the photospheric contribution to the emission assuming there is no excess emission at K.

The IRAS fluxes were taken from the Faint Source Catalogue, and the Point Source Catalogue when FSC fluxes were not available (i.e. for sources in the Galactic plane). This information was then compared with fluxes extracted using SCANPI (the Scan Processing and Integration tool) [2] which results in much reduced errors. This tool scans the raw IRAS data and averages individual scans to determine the point source flux and error of the object in question (as determined by coordinates) in each of the IRAS bands (12, 25 60 and 100 μm). The fluxes using different extraction methods could thus be analysed to give an independent determination of the significance of any excess measured to see if e.g., problems with background subtraction were affecting the results. Colour-correction was applied to the fluxes at the levels described in the IRAS Explanatory Supplement [3]. Specifically colour-correction applied to the 12, 25, 60 and 100 μm fluxes was 1.43, 1.40, 1.32 and 1.09 respectively. For stars with effective temperatures greater than 7000K (as determined by Kurucz profile fitting), colour corrections of 1.45 and 1.41 at 12 and 25 μm respectively were applied. The colour-correction was applied

[1] The sample stars are listed in the Debris Disk Database at http://www.roe.ac.uk/ukatc/research/topics/dust.

[2] http://scanpi.ipac.caltech.edu:9000/

[3] The IRAS Explanatory Supplement is available at http://irsa.ipac.caltech.edu/IRASdocs/exp.sup/

only to the stellar component of emission, through multiplication of the expected stellar flux by the colour-correction factor before subtraction to determine the excess emission. No further colour-correction was applied to the excess emission. The proximity of the IRAS sources to the stars was also checked given the quoted uncertainty error ellipse, since some surveys allowed excess sources to be up to 60 arcsec offset and have since been shown to not be related (Sylvester and Mannings 2000).

The final sample consisted of 11 stars of spectral types F, G and K and these are listed in Table 1. HD12039, not included in the IRAS catalogues, was identified as a warm dust host by Hines et al. (2006), and included in the later stages of this study.

3. Observations and Data Reduction

3.1. Observations

The observations were performed using a combination of: the Thermal Infrared MultiMode Instrument TIMMI2 on the ESO 3.6m telescope at La Silla; VISIR, the VLT Spectrometer and imager for the mid-infrared on the ESO VLT; and MICHELLE on Gemini North.

All of the observations employed a chop throw of 10″in the North-South direction (except for the MICHELLE observations for which the chop is 15″, and the chop throw was at 30°). Telescope and sky emissions were removed by an additional nod throw of the same size, taken in the perpendicular direction for TIMMI2 and VISIR, and in the parallel direction to the chop for the MICHELLE observations.

For the observations performed in perpendicular mode, this means that a straight co-addition of the data results in an image with two positive and two negative images of the source. The parallel chop-nod technique results in one central positive image and one negative image at half the level of the central image on either side in the throw direction. A residual dc (dark-current) offset was removed by subtracting the median in each column of the array and then in each row (the areas around the source images are masked off when determining these medians). The resulting images showed statistical uncertainty varying by just a few percent across the central 20 square arcsecond region around the images for all instruments. Bad pixels were determined by looking at the variations in individual chop frames, first creating 'empty' images in which only the half of a frame not containing the source would be used, together with the opposite half of the frame from the following nod position (which would also be empty). Pixels with a variance across the frames of 10 times more than the average were labelled 'bad' and masked off. Regions towards the edge of the array were found to be particularly prone to such variations, and were masked more frequently. Typically this stage would remove a few percent of pixels ($\sim$ 1000, array 320x240 or 256x256). This was also used to determine the variation of the sky during the observation, and in turn to determine the responsivity of individual pixels, so creating a gain map (in a perfect detector gain for all pixels would be 1). Note that in determining the gain map the regions on which the source emission fell on the detector would be masked off, as due to the chop and nod pattern the pixels would be unevenly illuminated in different nod frames and this would lead to inaccuracies in determining the gain map. Any pixels showing a particularly high or low gain ($< 2/3$ or $> 3/2$) were masked off. This would on average remove a few tens of pixels in addition to the previous masking. In total an average of around 7% of pixels were removed in the TIMMI2 observations, and around 4% of pixels in the MICHELLE and VISIR observations. This level was much reduced within the on-source apertures used to $\lesssim 1\%$, as most of the problem pixels were confined to the edges of the arrays, or to other regions which were avoided when deciding where to have the objects' images on the array.

In order to minimise the effects of changing conditions and airmass, calibration observations were taken of standard stars within a few degrees of the science object, immediately before and after each science observation whenever time constraints permitted. The standards were chosen from the list of K and M giants identified by Cohen et al. (1999). In addition to photometric calibration, these standards were used to characterise the PSF and used for comparison with the science sources to detect any extension (see section 3.2).

3.1.1. TIMMI2

The observations on TIMMI2 were taken over three runs on 11-12 September 2003, 19-21 November 2003 and 24-26 January 2005 (proposals 71.C-0312, 72.C-0041 and 74.C-0700). The conditions on these nights were very different. In particular observations performed in January demonstrated poor photometric accuracy. For the nights in which accurate photometry was not possible, it was still possible to place constraints on possible companion/background sources and extension with the data.

A wide range of the instruments filters were used to study this sample (M, N1, N2, 9.8, 11.9, 12.9). The pixel scale was 0.″3 for the M band and 0.″2 for the longer wavelengths, giving fields of view of 96″ x 64″ and 64″ x 48″ respectively. The FWHM was 0.″80 ± 0.″12 in the N band.

Absolute pointing of the telescope is accurate to 5-10″. However, pointing accuracy of 1″could be achieved by performing acquisition at M (which almost always detects the stars) and accounting for offsets between the filters by observations of the standards.

3.1.2. VISIR

The VISIR observations were carried out over three nights in December 2005 (proposal 076.C-0305). The conditions were good over all three nights, and allowed good photometric accuracy. The seeing was somewhat variable, with FWHM for standards in N band of 0.″465 ± 0.″161, and in the Q band 0.″597 ± 0.″166 over all observations. The PSF showed typical ellipticities of 0.18 and 0.1 in N and Q respectively. The same ellipticity was seen at the same position angle (regardless of on-sky chop angle) in the science and standard images and this instrumental artifact was well accounted for using the standard star images as model PSFs (see section §4).

Table 1. The Sample

Star name HD	Stellar type	Age Gyr	Distance pc	IRAS fluxes (mJy)[a] 12μm	25μm
10800	G1/2V	7.6[b]	27.1	479 + 15 (20)	113 + 82 (18)
12039	G3/5V	0.03[c]	42.4	Not in IRAS database[c]	
53246[d]	G6V	O(0.1)[e]	36.5	82 + 293 (30)	19 + 143 (26)
65277[d]	K4V	4.2[f]	17.5	184 - 46 (27)	43 + 83 (29)
69830	K0V	2[g]	12.6	603 + 77 (26)	142 + 171 (33)
79873[d]	F3V	1.5[b]	68.9	157 - 21 (25)	37 + 95 (38)
η Corvi[h]	F2V	1.3[b]	18.2	1212 + 412 (42)	283 + 420 (50)
123356[d]	G1V	O(0.1)[e]	20.9	14 + 1270 (53)	3 + 615 (56)
128400	G5V	0.3[i]	20.4	260 + 178 (24)	61 + 64 (23)
145263	F0V	0.009[j]	116.3	19 + 422 (50)	4 + 583 (35)
191089	F5V	0.1[k]	53.5	101 - 34 (29)	24 + 287 (55)
202406	F2IV/V	0.002	429.2	53 + 233 (33)	13 + 272 (48)

Notes: [a]=Fluxes are shown as star + excess (error), for HD65277 the 12 μm IRAS photometry suggests a lower flux than is expected from the photosphere, and so the excess is shown as negative; [b]=Age taken from Geneva-Copenhagen Survey; [c]= Identified as having excess by Hines et al. 2006; [d]= Binary object, see individual object descriptions, section §5; [e]=Age estimated by placing on colour-magnitude diagram following the work of Song et al. 2000; [f]=Age taken from Valenti & Fischer (2005); [g]=Beichman et al. (2006); [h]=HD 109085 also has excess at 60 and 100 μm; [i]= Age from Gaidos (1999); [j]=Honda et al.(2004); [j]=Age from Zuckerman & Song (2004).

Two filters were used for the observations; the N band filter SiC with central wavelength 11.85 μm (bandwidth 2.34 μm) and Q band filter Q2 with central wavelength 18.72 μm (bandwidth 0.88 μm). The pixel scale used was 0.″075, giving a 19.″2x19.″2 field of view. Observations of standards were performed before and after each observation, and standard observations were used throughout the night to determine an airmass correction. Calibration accuracy was 4% and 8% in N and Q respectively. Acquisition was performed in the N band for all stars. Chopping and nodding were performed in perpendicular mode as described above. The detector array for the instrument had several regions of very poor gain that were masked out by both the pipeline and our own reduction procedures, which required careful positioning of the stellar image on the array, particularly when also trying to image companion objects.

3.1.3. MICHELLE

MICHELLE observations of η Corvi were performed in service mode and taken on December 31st 2005 under proposal GN-2005B-Q15 with filter Si-5 (11.6μm, bandwidth 1.1μm). The detector array is 320x240 pixels, with pixel scale 0.″099 (resulting field of view is 31.″68x23.″76). The FWHM of the standards was 0.″35± 0.″02.

An average of the two observations of the standard was used for calibration, with an uncertainty of ±5.5% in calibration factor found between them. No airmass correction was necessary as the objects were observed at very similar airmasses (1.3-1.25). As guiding is only possible in one of the chopped positions with MICHELLE, one of the chop beams was always much less resolved than the other, giving an image of roughly twice the Full Width at Half Maximum (FWHM) found for the guided beam. Only the guided beams were included in our analysis.

3.2. Photometry and Background/Companion Objects

The result of the data reduction was an image for each observation consisting of four images of the target star (two positive, two negative) if observed in perpendicular mode, or three images of the target (one positive, two negative at half the level of detection) if observed in parallel mode. The multiple images were co-added to get a final image by first determining the centroid of each of the individual images. Photometry was then performed using a 1″ radius aperture for the TIMMI2 images and a 0.″5 radius aperture for the VISIR and MICHELLE images. These sizes were chosen to just exceed the full-width at half-maximum (FWHM) found for each instrument (as described in section 3.1). This minimises noise inclusion whilst including all the flux from an unextended source. Note that the filters used in these observations were narrow band and so no colour-correction was applied. Residual statistical image noise was calculated using an annulus centred on the star with inner radius the same as that used for the photometry, and outer radius of twice the inner radius (so 2″ for TIMMI2 and 1″ for VISIR and MICHELLE). Typical levels for statistical noise at the 1 σ level in a half hour observation were 44mJy total in the 1.″0 radius aperture of TIMMI2, 4 mJy and 12mJy for the 0.″5 aperture of VISIR in N and Q respectively, and 6mJy in the 0.″5 aperture of MICHELLE.

Smaller apertures were used to search for background sources and to place limits on detected sources. The aperture sizes were chosen to maximise the signal to noise of a point source in the aperture as determined by testing the standard star observations. The sizes of aperture used were 0.″8 in radius for the TIMMI2 observations, 0.″4 for MICHELLE, and 0.″32 and 0.″35 for the N and Q filters for VISIR. Apertures systematically centred on each pixel of the array in turn were searched for significant signal at the 3 σ level or above (based on the statistical noise). Where none were found, the limits placed on the background object were based on the 3 σ uncertainty in the aperture plus calibration uncertainty. For the non-photometric

nights, limits were based on calibration to the IRAS flux of the object. The upper limits to background sources are listed in Table 2.

4. Extension testing

An important part of this study was to look for evidence of extension in the observation images, or use the lack of extension to place limits on possible disk structure around the stars. For all observations we fitted a two-dimensional Gaussian to detected sources and compared the science image fit to the found for the standard stars. In addition for all observations the sources surface brightness profile was determined by calculating the average surface brightness in a series of annuli centered on the source of 2 pixel thickness by increasing inner radius from 0 to 3″ . The resulting sizes and profiles for all science observations were compared with those of the standards observed immediately before and after the science observations to search for any discrepancies in width.

To assess whether there is any evidence of extension in the science image the images of the point-like standard stars scaled to the peak of the science observation were used to model what an unextended source would be expected to look like. A straight-forward subtraction of the model from the science image was then performed and the resulting image subjected to a test to check for consistency with noise levels as measured on the pre-subtraction stellar image. Tests optimised for varying disk geometries were applied, choosing those that would give the highest signal-to-noise detection should such disks exist, as outlined in the following section. Note that since the PSF is scaled to the peak, then if the disk contributes to the peak some of the disk flux has been removed. Essentially we are testing the null hypothesis that the source is unextended.

4.1. A new method of determining extension limits

Here we consider what levels of disk flux could be detected in an observation, given its geometry. To do so we made model images of an unresolved star, at a level $F_\star$, and a disk at a level $F_{\rm disk}$, which we characterised by the parameter $R_\lambda = F_{\rm disk}/(F_\star + F_{\rm disk}) = F_{\rm disk}/F_{\rm tot}$ (see Figure 1 second column). The disk was assumed to be an annulus of radius r and width dr (so with inner radius $r - dr/2$, outer radius $r + dr/2$), with uniform surface brightness, at an inclination to our line of sight of I. These images were convolved with model PSFs (Figure 1 first and third columns). In this section we approximate the PSF by a Gaussian of FWHM θ, but in later sections we use the true observed PSFs. Models with $dr/r \in [0.2, 2.0]$, $r/\theta \in [0.083, 6.67]$, $I \in [0, 90]$, and $R_\lambda \in [0.001, 0.99]$ were tested. A best estimate of the unresolved contribution to the image was removed by subtracting a PSF scaled to the peak surface brightness (centered on the star, Figure 1 forth column). The optimum aperture that would be able to detect the residual disk emission given the uncertainties inherent in the observing process is then determined (Figure 1 fifth column). This optimal region has area $A_{\rm op}$.

We considered two sources of noise that hinder a detection. The first is the background noise on the array, which we assumed is Gaussianly distributed and which increases $\propto t^{0.5}$ for longer integrations. This leads to an increase in the S/N on the source $\propto t^{0.5}$ (signal increasing $\propto t$). This was characterised by $S_\star$, the signal to noise achieved on a flux $F_\star$ within an aperture of radius θ, and area $A_\theta = \pi\theta^2$, where the noise per pixel is assumed to be the background noise that is found across the array. Note that here we have ignored the photon noise contribution to the statistical noise term. This is because when searching for residual emission after the point source subtraction the flux is likely to be faint and thus background limited. Any noise caused by incorrect subtraction of the point-source is included in the second component of the noise described below. The definition of R_λ thus implies that the signal to noise on the disk flux in the same aperture is $S_\star(R_\lambda^{-1} - 1)^{-1}$ if $F_{\rm disk}$ lies entirely within the aperture. Note that $S_\star$ does not necessarily equate exactly with quoted instrumental sensitivities for which the region used for optimum detection must be considered. The second is the uncertainty in the PSFs due, e.g., to changes in the atmosphere which we characterise by the uncertainty in the FWHM $d\theta$ leading to uncertainties in the flux in an optimal region of size $A_{\rm op}$ of $N_{d\theta}$. These uncertainties were quantified as the difference in the flux in that optimal region when the PSF was changed from θ to $\theta + d\theta$. We tested $d\theta/\theta \in [0., 0.1]$. These noise sources were added in quadrature so that the final signal to noise in a region of area $A_{\rm op}$ is

$$S_{\rm op} = F_{\rm op}/N_{\rm op} = F_{\rm op}/\sqrt{(A_{\rm op}/A_\theta)N_\star^2 + N_{d\theta}^2} \quad (1)$$

where $N_\star = F_\star/S_\star$ is the background statistical noise in the aperture (A_θ) used on the point source. Here $F_{\rm op}$ is the flux in the optimal region, which assuming accurate subtraction of the stellar component in the PSF subtraction should be some fraction of $F_{\rm disk}$, and $N_{\rm op}$ is the noise in this same optimal region.

For any given geometry, a broad range of aperture parameters was considered and the one that gave the highest signal-to-noise detection as defined in equation 1 was chosen. We consider a detection to be where $S_{\rm op} > 3$.

4.1.1. Face-on ring

Here we consider the results of the modelling when applied to face-on rings. For large disks the symmetrical nature of a face-on ring means that the optimum region will be a ring of radius R, and width Δ, so that $A_{\rm op} \approx 2\pi R\Delta$. However, for disks close to or smaller than the size of the PSF ($r/\theta \ll 1$), we find that PSF accuracy is often the limiting factor. The optimal region for detecting residual extended emission would tend to a circular aperture. Using the R, Δ notation we note that when $R - \Delta/2 < 0$ the inner radius of the annulus becomes zero and the optimal region becomes a circular aperture of radius $R + \Delta/2$. For the face-on disk case we find

$$\begin{aligned} R/r &= 1 + 0.5(r/\theta)^{-1}(d\theta/\theta)(dr/r) \\ \Delta/r &= \sqrt{(dr/r)^{2-5(d\theta/\theta)} + (1.47 - (d\theta/\theta))(r/\theta)^{-2.3+10(d\theta/\theta)}} \\ F_{\rm op} &= (1 - (d\theta/\theta)^2(r/\theta)^{-2}R_\lambda^{-1})10^{-0.1(r/\theta)^{-1}}F_{\rm disk} \\ N_{\rm op} &= \sqrt{(A_{\rm op}/A_\theta)N_\star^2 + N_{d\theta}^2} \quad (2) \\ N_{d\theta} &= (d\theta/\theta)(dr/r)^{-1}10^{-10(r/\theta)}R_\lambda^{-0.5}F_{\rm tot} \end{aligned}$$

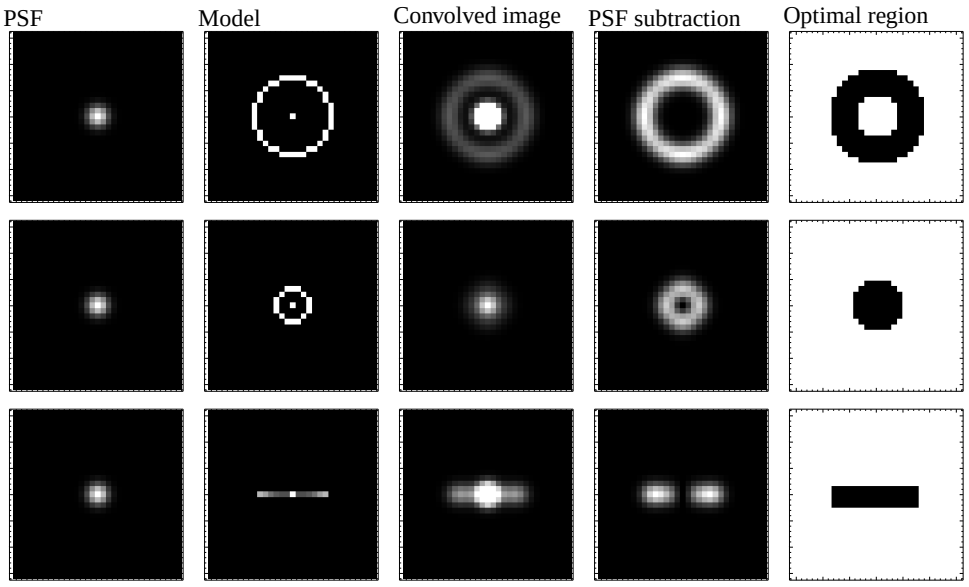

Fig. 1. Examples of the models tested and the various stages used to determine the optimal testing regions for detecting extended emission. The rows show three different models:*Top:* Face-on, large radius *r*; *middle:* Face-on small radius *r*; *bottom:* Edge-on large radius *r*. The model images (second column) are convolved with a PSF (first column), here approximated by a Gaussian to give the convolved images (third column). The point-like component of the final image is then removed by subtracting the PSF scaled to the peak of the convolved image (forth column). Finally a range of possible regions to test for residual emission are determined by finding the shape and size of a region that maximises the S/N on any residual emission on the array (black region, fifth column).

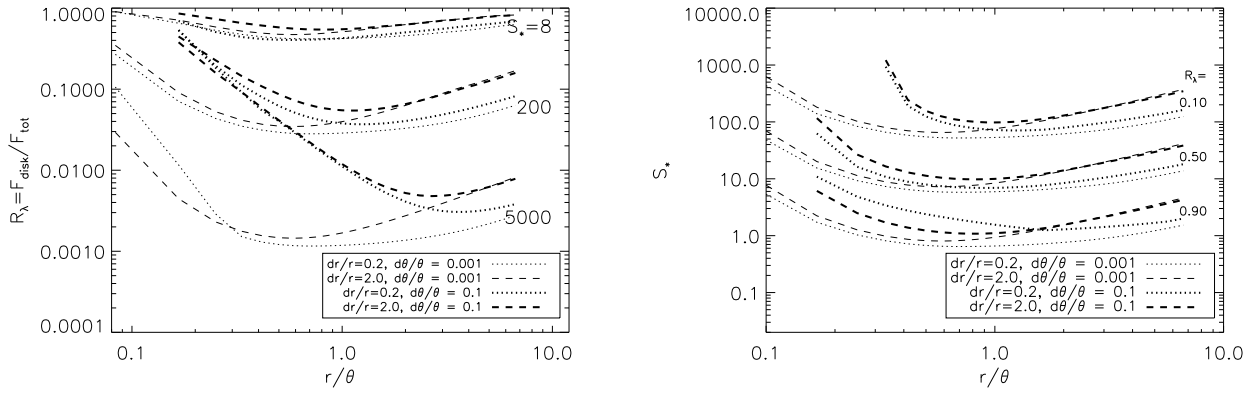

Fig. 2. Limits on detectable face-on disks for varying disk parameters. The region above the lines represents the region of detectability. Left: The disk flux required to get a 3 sigma detection of extension for disks of varying geometry in a face-on orientation (disk flux given in terms of R_λ, $F_\star = 10$ in these plots) Right: The signal-to-noise required for a significant detection for varying R_λ.

with $S_{\rm op}$ determined from equation 1. With these equations we can fit the numerical results for $S_{\rm op}$ to better than ± 50% for 85% of the disks models tested.

Notice that if the disk is large ($r/\theta \gg 1$) or the PSF perfectly known ($d\theta/\theta = 0$) then $N_{d\theta} = 0$ and $N_{\rm op} = \sqrt{(A_{\rm op}/A_\theta)N_\star^2}$. Also when $r/\theta \gg 1$, $F_{\rm op} \simeq F_{\rm disk}$ and

$$S_{\rm op} \simeq S_\star(\theta/r)(2\Delta/r)^{-0.5}(R_\lambda^{-1} - 1)^{-1}. \quad (3)$$

The required levels of R_λ as a function of r/θ and disk geometry to get a significant detection ($S_{\rm op} > 3$), as well as the signal required for a detection for a given R_λ are shown in Figure 2. These plots show the fitted functions given in equations 2. As mentioned above these functions fit the numerical results to better than ± 50% for 85% of the disk models tested.

The main features of the plots can be understood as follows: As can be seen in the equation for $F_{\rm op}$ (equations 2) the signal falls to zero when $r/\theta < (d\theta/\theta)R_\lambda^{-0.5}$. Thus even when the disk emission completely dominates the signal ($R_\lambda \simeq 1$) we cannot detect an extended disk to a smaller size than the uncertainties on the PSF. The optimal size of a disk in terms of ease of detectability (minimal required R_λ and $S_\star$) is $r/\theta \simeq 1$. This is easily understood from an intuitive point of view, as larger disks $r/\theta > 1$ have their flux dispersed over a wider area and so have reduced surface brightness making them harder to detect ($S_{\rm op} \propto (r/\theta)^{-1}$, equation 3), and smaller disks are more adversely affected by errors in PSF subtraction ($N_{d\theta} \propto 10^{-10(r/\theta)}$, equations 2), as well as by losing a large percentage of the disk flux in the peak-scaled point source subtraction ($F_{\rm op}/F_{\rm disk} \propto 10^{-0.1(r/\theta)^{-1}}$,

equations 2). Similarly in the large disk case wider disks are more difficult to detect as they have a lower surface brightness (the statistical noise over the optimal region will be higher as $(\Delta/r)^2 \propto (dr/r)^2$). The sharp fall-off of $N_{d\theta}$ with r/θ also explains why this error term can be neglected in the case of large face-on disks, and why for $r/\theta \gg 1$ the required R_λ (or $S_\star$) for detecting extension with large or small $d\theta/\theta$ tend to the same limits. The dependence of $N_{d\theta} \propto d\theta/\theta$ (equations 2) means that for smaller disks a higher uncertainty in the PSF has a strong effect in reducing the detectability of a disk (disks of a given geometry require much higher R_λ or alternatively higher $S_\star$ to be detected). Notice also that as $N_{d\theta} \propto (dr/r)^{-1}$, when PSF error dominates over statistical noise wider disks are easier to detect as less of the disk flux is lost in PSF subtraction and more disk flux may fall outside the region of PSF uncertainty.

In the small disks limit there are two contributions to the noise term $N_{\rm op}$, $N_{d\theta}$ from the PSF uncertainty and $\sqrt{A_{\rm op}/A_\theta}N_\star$ from the statistical noise in the optimal region. A high signal to noise will mean that $N_{\rm tot} \simeq N_{d\theta}$ for small disks, as can be seen by the convergence of the disk detectability limits with $S_\star = 200$ and 5000 when r/θ is small. Conversely when $S_\star$ is low the statistical errors can dominate even in the small disk limit and there is little difference in the detectable disk limits for small or large $d\theta/\theta$, as can be seen in the limits for $S_\star = 8$. The dominance of $N_{d\theta}$ for small disks and large $S_\star$ means that for small disks there is a limit at which detectability cannot be improved by increased observation time (increased $S_\star$). We can identify this point by considering when $N_{d\theta} > \sqrt{A_{\rm op}/A_\theta}N_\star$, i.e. when $N_{\rm tot}$ is dominated by PSF errors. Using $N_{d\theta}$ as given in equations 2 we can see that $N_{d\theta}$ dominates when

$$S_\star > \frac{\sqrt{A_{\rm op}/A_\theta}(dr/r)10^{10(r/\theta)}}{d\theta/\theta}R_\lambda^{0.5}(1-R_\lambda). \quad (4)$$

4.1.2. Edge-on ring

For an edge-on ring the optimum region can be modelled by a rectangular box with side lengths in the major and minor directions of $L_{\rm maj}$ and $L_{\rm min}$ respectively. The orientation of the major axis is that of the edge-on disk, which in testing the model limits is known as we know the input model. In the testing of actual source images for a disk, all orientations of major axis should be tested. We find

$$\begin{aligned} L_{\rm maj}/r &= 2\sqrt{2(dr/r)^{0.5} + 0.5(r/\theta)^{-2.7} + 10R_\lambda(d\theta/\theta)(1+r/\theta)^{-2}} \\ L_{\rm min}/r &= 2\sqrt{0.007(dr/r)^{0.5} + (0.3-0.8d\theta/\theta R_\lambda)(r/\theta)^{-2}} \\ F_{\rm op} &= (1-(d\theta/\theta)^2(r/\theta)^{-2}R_\lambda^{-1})10^{-0.25(r/\theta)^{-1}}F_{\rm disk} \\ N_{d\theta} &= 0.1(d\theta/\theta)10^{-10(r/\theta)}R_\lambda^{-0.5}F_{\rm tot} \end{aligned} \quad (5)$$

with $N_{\rm op}$ and $S_{\rm op}$ determined from equation 1. With these equations we can fit the numerical results for $S_{\rm op}$ to better than ± 50% for 80% of the disk models tested. Notice that as with the face-on disks when r/θ is large $F_{\rm op} \simeq F_{\rm disk}$ and we have

$$S_{\rm op} \simeq S_\star(\theta/r)(R_\lambda^{-1}-1)^{-1}/\sqrt{L_{\rm maj}L_{\rm min}/\pi r^2}. \quad (6)$$

The required levels of R_λ as a function of r/θ and disk geometry to get a significant detection, as well as the signal required for a detection for a given R_λ are shown in Figure 3. In general the detectability limits for an edge-on disk follow a similar pattern to the limits for a face-on disk, as can be seen in the similarity between figures 2 and 3. The differences can be understood as follows: The increased R_λ or $S_\star$ required for a significant detection is less steep in r/θ than for the face-on case because in the edge-on case the loss in surface brightness with increasing disk radius is slower than for a face-on disk. Thus for a fixed θ, the signal to noise will be generally higher in the edge-on geometry than for a face-on disk. Also in the edge-on case there is no dependence of $N_{d\theta}$ on dr/r, and so for small disks there is little difference between the detectability of wide and narrow disks. Errors will be dominated by PSF uncertainty (through $N_{d\theta}$) in the small disk case provided

$$S_\star > \frac{\sqrt{A_{\rm op}/A_\theta}10^{10(r/\theta)}}{10(d\theta/\theta)}R_\lambda^{0.5}(1-R_\lambda). \quad (7)$$

4.1.3. Inclined Ring

The case of an inclined disk, not edge on, falls between these two extrema, and the optimal region can be determined by interpolation between the two models dependent on the sine of the disk inclination, $\sin(I)$. The signal to noise for an inclined disk, and thus the disk flux required for a detection for a given observation, also follows a smooth transition between the two extremes.

4.1.4. Summary

The equations and figures in this section can be used as a guide to what disks may be detectable as extended sources in single dish imaging. The plots of R_λ vs r/θ for different sensitivity of observation (characterised by $S_\star$) can be used to provide guidelines as to how bright a disk must be compared to the star to be detected for different geometries. Any disks lying below the lines shown cannot be detected as extended sources, thus if an observation shows no evidence of extension, the area below the lines of detectability give the region of the parameter space in which the disk can lie. The plots of $S_\star$ vs r/θ can be used to determine the required observational time to resolve a disk in terms of the signal to noise required on the point-like star (combined with knowledge of the instrumental sensitivity and an approximation of the PSF) if the disk parameters are known or can be approximated (for example from SED fitting). Predictions based on these models for the resolvability limits acheivable with 8m telecsopes and comparison with already resovled disks will be included in a forthcoming paper (Smith & Wyatt in prep.).

The limits that can be placed on the extension of a disk for a given observation are dependent upon having a measure of R_λ. Often the disk flux is poorly constrained by the photometry, and so this limits the accuracy to which the possible extent of the disk can be constrained. If the disk flux is well known, then there are essentially two regimes when determining the detectability of disk extension. When $r/\theta > 1$, variations in the PSF have little effect on the optimal region and the signal to noise therein, and extension detection is limited purely by the background statistical noise on the array. When $r/\theta < 1$,

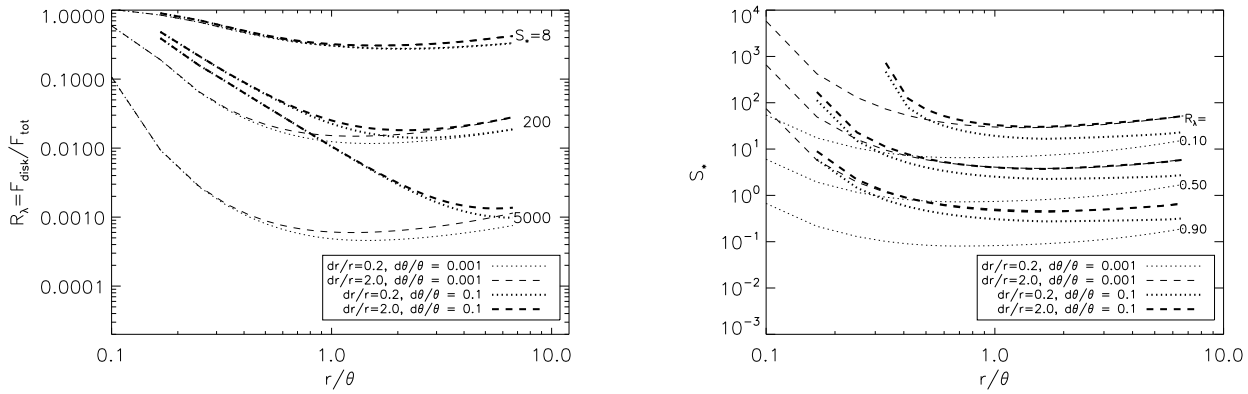

Fig. 3. Limits on detectable edge-on disks for various disk parameters. The region above the lines represents the region of detectability. Left: The disk flux required to get a 3 sigma detection of extension for disks of varying geometry in an edge-on orientation (disk flux given in terms of R_λ). Any disk above the line of detection would be detected at a significant level. Right: The signal-to-noise required for a significant detection for varying R_λ.

the variation in the PSF dominates the noise through the $N_{d\theta}$ term, and thus disk detections are limited by the degree of certainty to which the PSF can be characterised. A disk cannot be detected to a smaller size than the absolute errors in the PSF, or obviously to smaller than the pixel scale of the images, regardless of the signal strength of the observation. We acknowledge that we are in affect talking about super-resolution of the disks, as in our models we can detect extension just larger than a single pixel scale if the PSF is perfectly known. In reality however, variation in the PSF both in terms of absolute width and variation in shape will severely restrict the possibility of resolving disks of this size. Figures 2 and 3 also show that the optimal disk size for detectability changes from $\sim r/\theta$ when $d\theta/\theta$ is very small to larger radii with larger and more realistic values of $d\theta/\theta$. It is worth reiterating that the value of θ does not encompass all of the information about the PSF, in particular any asymmetries or ellipticity $\neq 0$ can affect extension limits, therefore when determining the limits placed on the observed sources in this paper, we used the PSF determined for each source. For disks smaller than the limits to which we may reasonably expect a stable and unvarying PSF, single aperture imaging will be unable to resolve the disk and interferometric observations will be needed.

5. Results and Analysis

The observed sample can be divided into several sub-groups: main sequence stars with confirmed hot dust; hot dust hosts that have been incorrectly identified as main sequence objects; and those with no excess or whose infrared excesses are actually due to background/companion objects or statistical anomaly. Table 2 gives a brief description of the results, and Table 3 gives the best fits to the objects for which the excesses are confirmed. Sources are discussed individually below.

5.1. Confirmed hot dust around η Corvi

The results confirm the presence of excess emission centred on the star toward η Corvi which was originally shown to have an infrared excess by Stencel & Backman (1991) based on the large infrared flux in the IRAS catalogue. The excess is 412 ± 42 mJy at 12 μm and 420 ± 50 mJy at 25 μm (Table 1). η Corvi also has a sub-mm excess, at an approximate temperature of 40K, which has been imaged by Wyatt et al. (2005) using SCUBA. The deconvolved size of this object is 100AU at 850 μm. The 450 μm image can be modelled by a ring at 150AU. The SED of this object, having a large mid-infrared excess shows evidence for a hot component in addition to the cool 40K component. However it is not clear if the hot component is at a single temperature of 370K, as modelled by Wyatt et al. (2005) or at two temperatures, 360K and 120K, as suggested by Chen et al. (2006)

This source was observed with TIMMI2 at 9.56 μm, 10.54 μm and 11.59 μm. The images at 11.59 μm have the greatest calibration accuracy and were previously reported in Wyatt et al. (2005). With these observations a background or companion source within the TIMMI2 field of view can be ruled out at the level of less than 76 mJy, indicating the excess is indeed centred on the star.

Further observations presented here using VISIR confirm the presence of excess emission at N and Q centered on the star at a level consistent with that detected by IRAS and Spitzer (Chen et al. 2006). The detected flux is 1951 ± 216 mJy and 814 ± 85 mJy at 11.85 and 18.72 μm respectively (photospheric emission expected to be 1243 and 505 mJy in these filters). The N band excess emission from the VISIR observation is higher than that of IRAS at 12 μm and IRS, but the large calibration error means that this difference is not significant. The MICHELLE observation also has a high calibration error: the detected flux is 1626 ± 184 mJy and so does not confirm the excess at the 3 σ level of significance (photosphere expected to be 1298 mJy). The limit on excess is in line with the IRAS measurements (see Table 1). These data points, together with the IRAS and SCUBA measurements of excess and the IRS spectra presented by Chen et al. (2006) are shown in Figure 4. The observations allow us to place limits on possible background companions within the field of view of the instruments to less than 28 mJy at N and less than 23 mJy at Q.

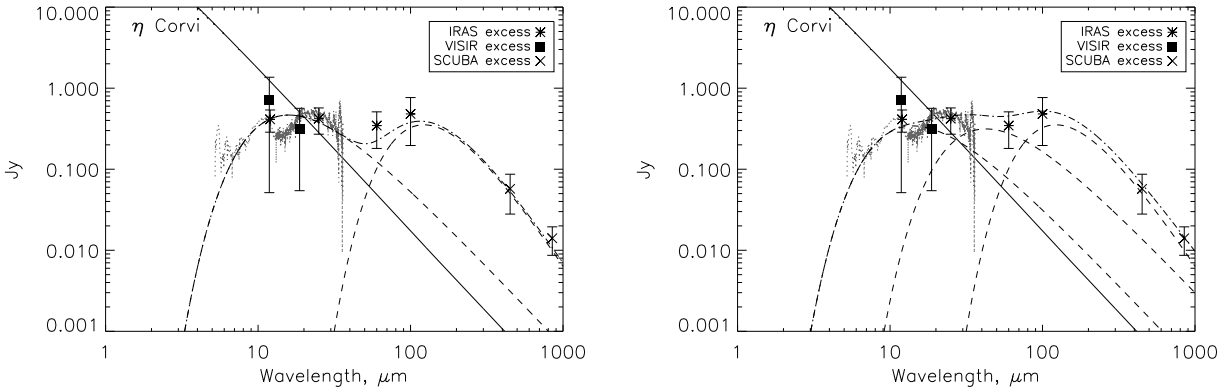

Fig. 4. The two alternative fits to the excess emission of η Corvi. The symbols > 10μm represent calibrated flux after subtraction of photospheric emission. Error bars are 3 σ. The grey dotted line represents the IRS spectra of Chen et al. (2006) after subtraction of the photosphere. The dashed lines indicate blackbody emission modelling of the disk flux, left: model A; and right: model B; and the dot-dashed lines the total emission from the multi-temperature disk.

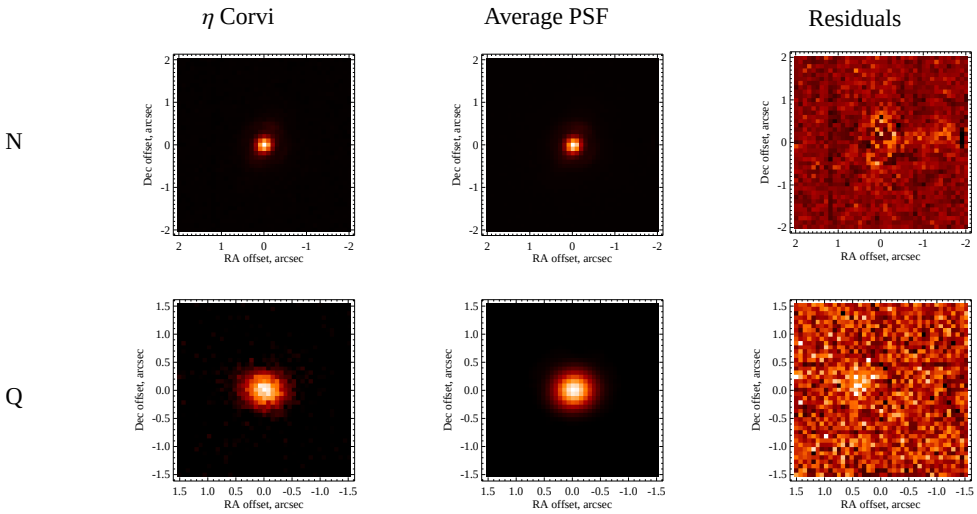

Fig. 5. The final images of η Corvi and the standard star associated with it, and the η Corvi image after subtraction of the scaled standard star image which is examined for residuals indicative of extended disk emission. *Top:* The MICHELLE N band images; *bottom:* the VISIR Q band images. All scales are linear. The images of the residual emission are shown with minimums (black) of -3 σ and maximum (white) of +3 σ (where σ is the background noise level per pixel). While the Q band residuals appear to show a 12σ peak to the East (determined in a 0.″35 radius aperture, see section 3.2), this emission does not appear after subtraction of the first standard star image only, which is broader than the standard star observation taken after observing η Corvi (signal in same aperture is 0.7σ).

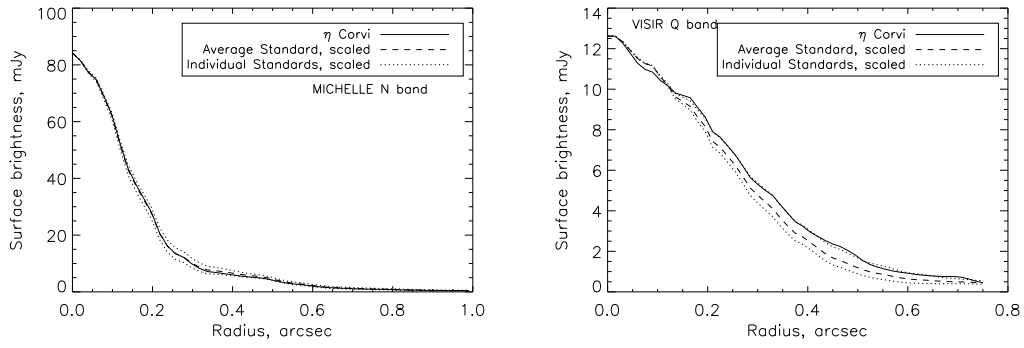

Fig. 6. The surface brightness profiles of η Corvi and the standard star images associated with the observations. Standard star profiles are scaled to the η Corvi profile. The profiles of η Corvi are consistent with those of the point-like standard stars.

Table 2. The Observations

Star name	Observation			Exp. Photospheric	Results[a]			
HD	λ, μm	Int. time, s	Instrument	Flux, mJy	Flux, mJy	Tot. Error, mJy	Stats. Error	Background limit, mJy[b]
10800	11.59	1800	TIMMI2	513	477	54	15	≤ 39
	18.72	3762	VISIR	200	186	29	6	≤ 14
12039	11.85	3588	VISIR	72	77	3	1	≤ 2
53246	11.59	1800	TIMMI2	87	111	30	25	≤ 62
65277	11.59	2400	TIMMI2	197	197	38	11	≤ 31
	11.85	1794	VISIR	188	182	4	2	≤ 5
	18.72	3762	VISIR	77	78	14	4	≤ 10
Binary	11.59	2400	TIMMI2	55	33	17	11	/
	11.85	1794	VISIR[d]	53	32	5	2	/
	18.72	3762	VISIR[d]	21	14	6	4	/
69830	9.56	1980	TIMMI2	941	1255	135	32	≤ 84
79873	11.59	1800	TIMMI2	167	160	18	11	≤ 28
	18.72	1881	VISIR	65	39	9	5	≤ 12
Binary	11.59	1800	TIMMI2	14	0	11	11	/
	18.72	1881	VISIR	6	0	5	5	/
η Corvi	9.56	1620	TIMMI2	1896	2883	240	63	≤ 162
(109085)	10.54	3600	TIMMI2	1565	2451	373	48	≤ 84
	11.59	840	TIMMI2	1298	2151	127	40	≤ 76
	11.6	1244	MICHELLE	1296	1626	184	5	≤ 33
	11.85	1076	VISIR*	1243	1951	216	19	≤ 28
	18.72	1881	VISIR	505	814	76	10	≤ 23
123356	10.54	660	TIMMI2	[18][c] 681	207	78	64	≤ 164
128400	8.60	600	TIMMI2	498	469	92	41	≤ 109
	9.56	661	TIMMI2	406	507	118	61	≤ 162
145263	8.60	1380	TIMMI2	37	426	57	25	≤ 64
191089	12.21	1440	TIMMI2	98	92	27	16	≤ 43
202406	9.56	1800	TIMMI2	83	270	43	12	≤ 30
	11.59	1560	TIMMI2	57	278	54	16	≤ 43

The expected photospheric emission is determined by a Kurucz model profile appropriate to the spectral type of the star and scaled to the K band 2MASS magnitude as outlined in section 2 unless otherwise stated in the individual source description. Errors are 1σ. M band TIMMI2 observations were largely non-photometric and primarily used to improve pointing accuracy and thus are not listed in this table. Notes: [a] Errors are total errors (inclusive of calibration uncertainty and image noise). [b] Limits are 3σ upper limit to undetected object including calibration errors, or scaled to IRAS fluxes when conditions were non-photospheric. These limits are valid to within 28″of the detected source for TIMMI2 observations, 12.″6 for MICHELLE observations and 11.″4 of the source for VISIR observations. [c] Here the companion object is brighter than the primary; we show the primary flux in brackets; * This observation was affected by rising cirrus, and so levels of noise on the image are much higher than other observations taken with this filter.

The final images for η Corvi from the MICHELLE and VISIR Q band imaging are shown in Figure 5 together with the average PSFs obtained from the standard star observations and the residuals after subtracting the scaled average PSF from the science images. The average PSF was determined by co-addition of the individual images of the observed standard star. It is possible to assess the level of PSF variability during the observations since these bright sources can be easily characterised even in short integrations. Therefore we can compare the FWHM measurements from 2-dimensional Gaussian fits to sub-integrations of the observations, that is dividing the total dataset for any integration into shorter integrations of equal length, for both the standard stars and η Corvi. For the MICHELLE N band observation the standard images have a median FWHM of 0.″357 and standard error 0.″0024 (20 sub-integrations), and η Corvi a median FWHM of 0.″363 with standard error 0.″003 (24 sub-integrations). Note that the For the Q band observation with VISIR, the standard star FWHM observations had a median value of 0.″577 and standard error 0.″037 (4 sub-integrations) with η Corvi having a median FWHM of 0.″607 and standard error of 0.″018 (observation divided into only 3 sub-integrations to have adequate S/N to determine FWHM). Thus, based on the FWHM measurements the η Corvi images are not significantly larger than the PSF images (at either wavelength). Futhermore, the residual images were subjected to testing using a wide range of optimal regions as defined in section 4.1 to search for significant residual emission indicative of extension. No significant extension was found at either N or Q. The residual emission in the Q band residual image which appears to have ∼12sigma significance based on the ratio of signal to pixel-to-pixel statistical noise is not interpreted as extended emission, since such a calculation does not account for the uncertainty in the PSF. In fact, the PSF of the standard star observed before eta Corvi looks very similar to that of eta Corvi (see Figure 6), and when using this individual standard star observation (rather than the average) as the model PSF, the signal in the region previously highlighted for potential extension (centered on ∼ 0.″47, PA 71°), is reduced

Table 3. The fits for stars with confirmed excesses

Star name	Fit as dust disk			Limit on extension	$f_{IR} = L_{dust}/L*$	f^a_{max}
HD	Temp, K	Radius, AU	Radius, $''$	Radius	$\times 10^{-5}$	$\times 10^{-5}$
η Corvi	320	1.7	0.09	$<0\farcs164$ ($^{+0.014}_{-0.009}$)	26	0.042
(109085)	360 + 120[b]	1.3 + 12	0.07 + 0.66	-	22 + 6	0.022 + 4.01
145263[c]	290	1.8	0.015	$<0\farcs69\ ^{+0.31}_{-0.21}$	2033	7.0
202406[d]	290	7.4	0.025	$<0\farcs33^{+0.21}_{-0.13}$	371	22.9
12039	120[e]	5.05	0.12	-	8.9	23.3
69830	390[f]	0.33	0.026	-	25.4	0.0006
191089	110	11.5	0.21	-	233	47.4

Note that the objects with no extension limits have too low a fractional excess for the extension to have been detected in the images regardless of size. Estimates of radius are based on blackbody fits and could be up to three times larger than suggested (Schneider et al. 2006). Limits shown here are for a narrow face-on disk. Errors arise from 3 sigma photometric errors - see section 4.1.4. Horizontal lines indicate division into photometrical confirmed debris disks, suspected pre-main sequence stars, and sources for which our results provide constraints on the disks (sections 5.1, 5.2 and 5.3 respectively).

Notes: [a] see section 6.2 for details of this limit; [b] Fit suggested by Chen et al. (2006); [c] HAeBe Star ; [d] Possible HAeBE star, see section 5.2 ; [e] Fit from Hines et al. (2006); [f] Beichman et al. (2006) suggest Hale-Bopp type cometary material.

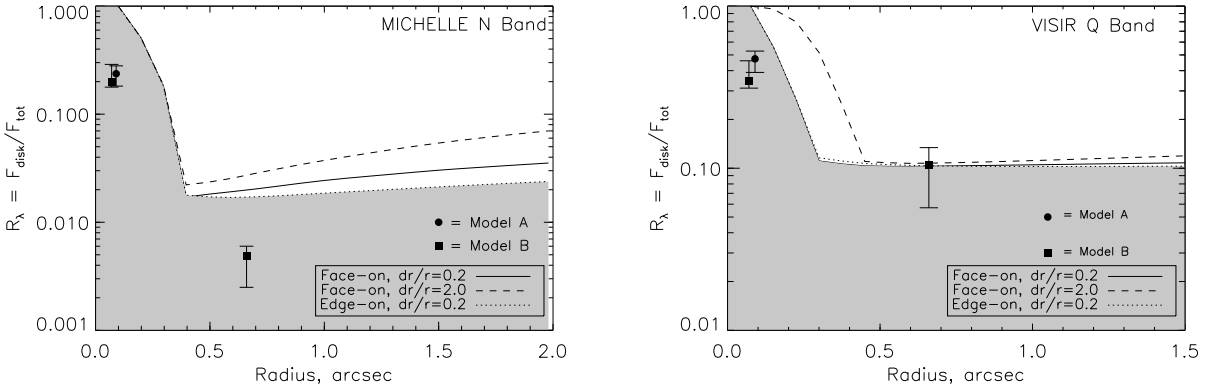

Fig. 7. The 3 σ limits placed on the disk models by non-detection of extension in the images. *Left:* The most stringent limits placed on possible disk radius at N are achieved with MICHELLE due to the poor seeing of the VISIR observation. The parameters used in determining these limits are $S_\star = 325$, $\theta = 0\farcs36$, $d\theta/\theta = 0.1$. *Right:* The extension limits given by the VISIR Q band imaging. The parameters used in determining these limits are $S_\star = 81$, $\theta = 0\farcs58$ and $d\theta/\theta = 0.08$. In both plots error bars represent the 3 σ errors on R_λ due to photometric uncertainty. The shaded area is the area in which disk populations could lie given the non-detection of extension. Note that the cold dust at 40K imaged in the sub-milimetre lies at approximately 45° to the line of sight, so between the edge-on and face-on limits presented here. See text for model details and the implications of these limits.

to 29 ± 37 mJy. Thus there is no extension beyond the uncertainty in the PSF. This illustrates the potential to mis-identify extended emission if PSF uncertainty is not taken into account.

The observed PSFs were then convolved with our range of disk models described in section 4.1 and these convolved images treated in the same way to test which set of disk parameters would have led to a significant detection in our optimal regions. Figure 7 shows the extension limits plots for the MICHELLE N band imaging (which due to better seeing provides more stringent limits than the VISIR N band imaging) and VISIR Q band imaging, which as discussed in section 4.1.4 are strongly dependent on the level of fractional excess, and thus on the number of disk temperatures used to fit the excess emission. We discuss these limits in the context of two possible interpretations, labelled model A and model B, in which the dust emitting in the mid-infrared is at either A: one temperature, or B: two temperatures, making the further assumption that each temperature corresponds to a different radius in the disk. To determine the limits the non-extension places on the different models the value of $R_\lambda = F_{\rm disk}/F_{\rm total}$ is crucial. In the following limits discussion, the value of R_λ adopted is derived from the IRS spectrum at the wavelengths of the images used (11.6μm and 18.72μm for MICHELLE N band and VISIR Q band images respectively), as this spectrum provides more accurate photometry than our ground-based observations. The blackbody fits shown on the SED plots in Figure 4 act as a guide to an approximate temperature and thus location of the dust populations. For model A the excess emission at both N and Q is assumed to come from a single component at a single location. For model B the blackbody fits have been used to give relative contributions to the emission at each wavelength from the two components. In both models the cold disk component imaged by Wyatt et al. (2005) is fit by a 40K blackbody, and does not contribute to the flux in the mid-infrared.

Model A: The IRS photometry suggests fractional excess of $R_\lambda = 0.24$ and 0.47 at N and Q. The extension limits show

that assuming a face-on narrow disk geometry, a single disk component must be at less than 0.″164 ± 0.″01 (from the tightest Q band limit, errors from uncertainty in R_λ from IRS spectra uncertainty), which translates to a radial offset of 2.98 AU. Assuming a wide ring geometry the limit is 0.″253 (4.6 AU, see Figure 7). Using a single temperature blackbody to fit the hot component we find that a fit of 320K is best suited to our interpretation of the IRAS measurements, slightly lower than the 370K found by Wyatt et al. (2005) (see Figure 4, left). The luminosity of this F2V star as fitted by a Kurucz profile (see section 2) is 5.5 $L_\odot$, and thus assuming that the emitting grains behave like blackbodies, dust grains emitting at 320K would be at a distance of 1.7 AU (0.″09). This small radial offset is consistent with the extension test limits. However there can be a difference of up to a factor of 3 between a blackbody fit and the true radial offset of a dust population (Schneider et al. 2006), thus the limits from these observations show that a single mid-infrared component is not likely to be much hotter than the blackbody fit of 320K (maximum of $\sim$ 1.3 or 1.6 times the blackbody temperature for narrow and wide ring geometries respectively).

Model B: The two components of the mid-infrared emission in this model have $R_{11.6\mu\mathrm{m}} = 0.20$ and $R_{18.72\mu\mathrm{m}} = 0.34$ for the dust at 360K and $R_{11.6\mu\mathrm{m}} = 0.005$ and $R_{18.72\mu\mathrm{m}} = 0.105$ for the dust at 120K, based on blackbody fits (see earlier in this subsection). The extension limits suggest an outer limit of 0.″19 ± 0.″02 for a narrow face-on ring (Q band limit) for the hot component assuming 3 σ limits (see Figure 7). This is consistent with the 0.″07 (1.3 AU) size predicted by a blackbody grain assumption. For the 120K component, the Q band limits greatly restrict the possible location of the disk. In fact at the predicted 0.″66 (12 AU) location from an assumption of blackbody dust grains, this mid-temperature component is ruled out at the 3.5 σ level assuming a narrow face-on ring. A narrow edge-on ring is also ruled out at a significance of 3.4 σ, as is a wide face-on ring at a lower significance of 2.6 σ although a wide edge-on ring is only ruled out at 2.3 σ. Note that from Figure 7 it can be seen that larger disks (within the factor of 3 expected from Schneider et al. 2006) are also ruled out at the $\gtrsim 2\sigma$ limit. Thus at a significance of $> 2\sigma$ these observations rule out this model for the mid-infrared excess emission of η Corvi. There remains some uncertainty in these limits, as these limits assume $R_\lambda = 0.105$ at Q for this dust component. Photometric errors and errors in determination of the relative contributions to the excess emission from the 370K and 120K components respectively at Q mean that this could be as high as 0.134, or as low as 0.057. These uncertainties include the uncertainty from the IRS spectra, although the dominant source of uncertainty in R_λ in this model is the poorly constrained relative contributions arising from the two components emitting at Q. A longer observation of this source at Q, with a signal to noise of at least double that achieved in these observations, would either resolve this component, or allow it to be ruled out at a more certain level of significance.

To summarise, the observations do not allow a certain differentiation between the two alternative models for the excess emission. At the 2.6 σ level (assuming a reasonably favourable disk geometry) we rule out the middle temperature component required by model B and thus the limits favour model A - a single hot component at 320K in addition to the cool 40K component already known. We were also able to set constraints on the radial extent of the model A fit and the hotter component of model B. These limits suggest that the radial size of the disk is at most 1.75 times that predicted from a blackbody interpretation for model A, or 2.7 times the blackbody prediction for the hottest component of model B. Deeper observations at Q are required to allow a clearer differentiation between the two models. Components at 320K or 360K (models A and B respectively) are expected to be smaller or comparable to the single pixel scale of VISIR and MICHELLE, and are unlikely to be resolvable on 8m instruments. Mid-infrared interferometry is the only tool that currently has the potential to resolve emission on such a small spatial scale.

5.2. Confirmed hot disks around young stars.

Two of the sample are also confirmed to have hot excess emission. However, on further investigation these are revealed not to be main-sequence stars of a similar age to the rest of the sample.

HD145263: The star was originally proposed as a debris disk hosting candidate in Mannings and Barlow (1998). It has an IRAS excess at 12 μm of 422 ± 50 mJy and at 25 μm of 583 ± 35 mJy (see Table 1). It was also studied by Honda et al. (2004) using Subaru/COMICS from 8-13 μm. No pointing error is quoted by Honda et al. (2004), but the blind pointing accuracy of the Subaru Telescope is less than 1″, and so it can be assumed that the crystalline silicate grains with a broad feature with shoulders at 9.3 and 11.44 μm seen in their spectrum are from a disk around the star. HD145263 is a member of the Upper Scorpius association, whose age is estimated to be 8-10Myr. It is close to the zero-age main sequence in the H-R diagram (Sylvester and Mannings 2000). The fractional luminosity as measured using the fits to the IRAS detections is $L_{IR}/L_* = 0.014$, smaller than is typical for T Tauri and HAeBe stars but larger than debris disk hosts (Honda et al. 2000 and references therein). Thus Honda et al. (2000) suggest this star could be considered a young Vega-like star.

The excess at 8.6 μm is confirmed with the TIMMI2 data, finding a flux of 426 ± 57 mJy (expected photospheric emission at this wavelength is 37 mJy). This result is consistent with the IRAS fluxes and also the spectra of Honda et al. (2004). The data place a limit on undetected background or companion sources of less than 64 mJy. Since the stellar photosphere would not have been detected, we can only confirm that the source is centered on the star to within 1″, the accuracy of the pointing. No extension is detected in the image of this source. Applying a blackbody fit to the excess emission gives a temperature of 290K (see Figure 8 left), and at this wavelength an R_λ of 0.88. Though the disk flux is bright, the radial offset of the dust is predicted to be 1.8AU, which at the distance of this star as measured by its parallax is only 0.″015 on-sky. Such a small disk is beyond the resolution limits of even the 8m class telescopes, and could only be resolved using interferometry (see e.g. Ratzka et al. 2007 for an example of a T Tauri star re-

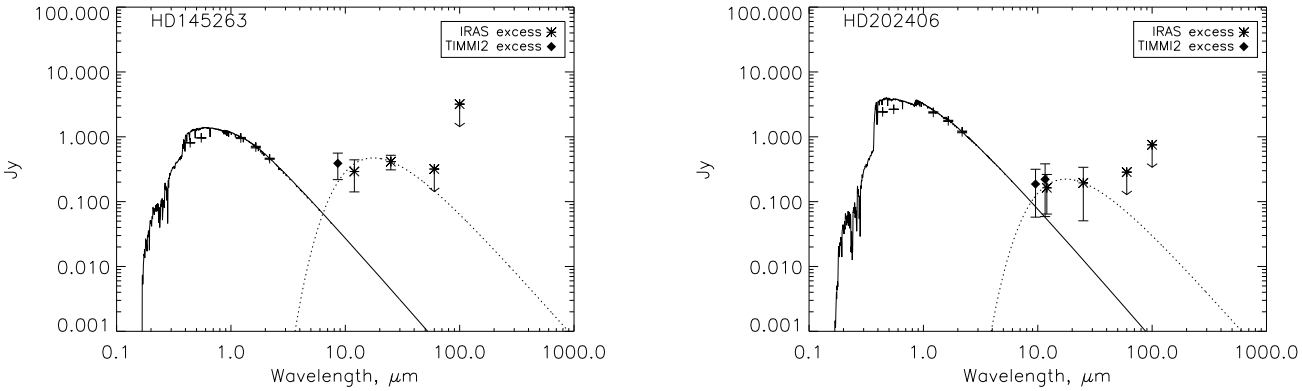

Fig. 8. The SEDs of the two young confirmed excess emission sources. The solid line gives the photospheric emission modelled by Kurucz atmospheres, and the flux levels plotted at > 10μm are measurements of excess after the subtraction of the photosphere. Limits and error bars are 3 sigma. Dotted lines are single temperature blackbody fits to the excess. The fits are described in Table 3.

solved using interferometry). The extension limits from these observations are only very weak (see Table 3).

HD202406: Oudmaijer et al. (1992) identified this object in a survey of SAO stars for IRAS excess. Its luminosity class in the Hipparcos catalogue is identified as IV/V. The parallax of this object is quite uncertain (2.33 ± 1.44 mas), and gives a distance to this object of 430^{+410}_{-142} pc, but assuming the star has the luminosity of a main sequence F2 star ($2.9L_{\odot}$) would imply a distance of only 63 pc, which is incompatible with the Hipparcos parallax. It is likely to be a subgiant or pre-main sequence object. There is no information in the literature about rotational velocity or spectral lines for this object to enable us to make a distinction between these two possibilities. However it does lie in the direction of a group of molecular clouds M46, M47 and M48, which lie at a distance of $\gtrsim$ 290 pc (Franco 1989). The proximity to this cloud region suggests the star is more likely to be a pre-main sequence star. We assume a distance of 300pc to be consistent with the molecular clouds implying that $L_{*} = 65L_{\odot}$ which we adopt in the following discussion. Using the stellar models of Siess et al. (2000) and taking an effective temperature of 7000K (appropriate for an F2 star) a likely age for this star is 1.6 Myr. This is in agreement with the evolutionary tracks of Palla & Stahler (1993) which suggest an age of 3 Myr for this object.

The TIMMI2 observations of HD202406 detect the excess emission centred on the photosphere at above 4 σ at 9.56 and 11.59 μm. The detected levels of flux at these wavelengths are 270 ± 43 mJy and 278 ± 54 mJy (photosphere expected to be 83 and 57) respectively. A limit of less than 30 mJy can be placed on any undetected background object at 9.56 μm, and less than 43 mJy at 11.59 μm. Fitting the excess emission with a blackbody gives a temperature of 290K (see Figure 8, right) which corresponds to a dust location of 7.4AU (0.″025). Note that should we have chosen a different stellar distance, the dust offset in arcseconds would be the same (due to an increased luminosity and thus radial offset of dust for the same temperature blackbody fit at increased distance). Given this small predicted size, it is unsurprising that no extension was detected in the images. Indeed the limit set from extension testing is less than 0.″33 radius for a thin ring around this source at $R_{11.59\mu m} = 0.81$, corresponding to a radius of 99 AU. The shape of the emission here has been modelled by a blackbody. However, at the level of 3 σ significance a simple power-law would fit this excess flux equally well. Thus we require limits on excess at shorter wavelengths to determine a grouping according to the scheme of Meeus et al. (2001) and differentiation between a flat and flared disk geometry. This in turn may indicate evolutionary status, as a dip around 10 μm is thought to develop and widen with age (see e.g. van den Ancker et al. 1997). It should be noted however that we derive a $L_{\rm IR}/L_{*}$ of 0.00371, which as for HD145263, is lower than typical T Tauri stars for which values of $L_{\rm IR}/L_{*} \sim 0.1$ are more typical (see e.g. Padgett et al. 2006). This may indicate that these objects are in a transitional stage.

5.3. Constraints on hot dust sources

HD69830: Mannings and Barlow (1998) used the IRAS database to identify an excess around HD69830 in the 25 μm band, at the level of 5 σ (142 mJy photosphere, excess 171 ± 33 mJy, see Table 1). There is no detection of excess at longer wavelengths, and an insignificant excess at 12 μm. SCUBA observations limit the excess at 850 μm to < 7 mJy (Matthews et al. 2007). Beichman et al. (2005) observed this object with the IRS and MIPS instruments on Spitzer and found further evidence for excess at 24 μm with MIPS, and between 8 and 35 μm with IRS. No excess was found at 70 μm. At 24 μm the excess was measured to be 70 ± 12 mJy (aperture 15″radius). The IRS spectra between 8-35 μm reveals the presence of crystalline silicates (see dashed line Figure 9, right). Interest in this source has intensified since the discovery of 3 Neptune mass planets at < 1 AU (Lovis et al. 2006).

Unfortunate conditions mean the measures of the N band emission of this object are non-photometric. The object is detected at a S/N of 39, and find a calibrated flux of 1255 ± 135 mJy using just the standard observations immediately before and after the science observation for calibration. As conditions were very changeable over the course of the night, this may

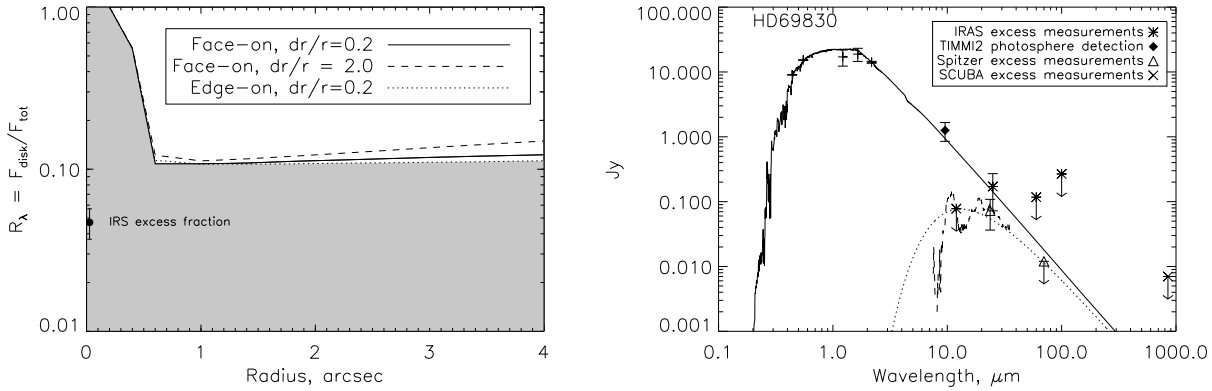

Fig. 9. Observations results for HD69830. *Left:* The extension testing limits for the observation of HD 69830. Note that at the measured level of fractional excess no limits can be placed on possible extension (fractional excess level and errors taken from IRS spectra). The predicted disk size is shown by an asterisk with error bars marking the 3 sigma photometric errors. The shaded area shows the possible disk location. Parameters used in determining these limits are $S_\star = 39$, $\theta = 0\farcs88$ and $d\theta/\theta = 0.1$. *Right:* The SED of this object, with excess measurements shown after the subtraction of the photospheric contribution. The blackbody fit to the excess shown by the dotted line and gives the predicted disk size shown in the left-hand Figure. The dashed line shows the photosphere subtracted Spitzer IRS spectra obtained by Beichman et al. (2005). Note the strong silicate features are obvious from this plot.

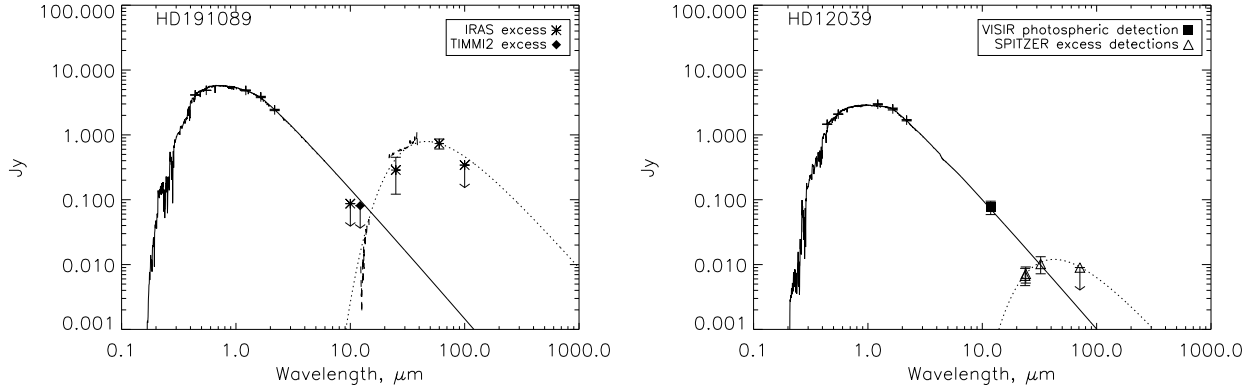

Fig. 10. The SED fits of objects with hot dust confirmed in the literature. For both objects the solid line is photospheric emission as modelled by a Kurucz profile. Symbols representing the excess measurements are the measured flux minus the photospheric emission as modelled by the Kurucz profiles. Error bars and upper limits are at the 3 sigma level. The dashed line on the plot of HD191089 is the publicly available low-resolution IRS spectra after photospheric subtraction originally presented in Chen et al. (2006). The dotted lines are blackbody fits to the dust emission with parameters described in Table 3.

mean the the errors are under-estimated. At this level of flux we are within 3 σ of the predicted photosphere at this wavelength (941 mJy at 9.56 μm). A 3 σ limit of 84 mJy can be placed on any background/companion object in the field of view, making it highly unlikely that the Spitzer photometric excesses obtained in a larger aperture are due to any such object. Thus we can be confident that the excess emission is centered on the star.

The source did not exhibit extension. The extension testing procedures were applied to this observation and the resulting detectability limits are shown in Figure 9 (left). The limits show that a minimum extended contribution of $R_\lambda = 0.107$ is necessary to place spatial constraints on the disk flux. The SED fit of a blackbody at 390K translates to a disk radius of 0.33AU ($0\farcs026$), with a fractional contribution to the excess of $R_\lambda = 0.05\pm\mathbf{0.01}$ at the wavelength of this observation seen in the IRS spectrum of this source (see Figure 9, right). This predicted disk model is shown on Figure 9 (left). Beichman et al (2005) suggest a disk radius of 0.5AU ($0\farcs04$). Also Lisse et al. (2007) model the IRS spectrum in detail and find a dust radius of $\sim$ 1AU ($0\farcs08$). However given the expected fractional flux contribution at N is only 5%, it is unsuprising that the disk is unresolved. The small spatial scale suggested by these models would require mid-infrared interferometry to resolve the emission (see section 4.1.4).

HD191089: HD191089 was identified by Mannings and Barlow (1998) as a debris disk candidate based on its IRAS photometry. This source has excesses of 287 mJy at 25 μm and 735 mJy at 60 μm at the 5 and 17 σ levels respectively (as noted in Table 1). At shorter wavelengths there was no excess detected by IRAS.

This object was observed at 12.21 μm with TIMMI2. The photosphere was detected at a signal to noise of 5.75. The pho-

tometry is consistent with the predicted photospheric emission (92 ± 27 mJy calibrated flux; Kurucz model profile predicts 98mJy from the photosphere). No other source was detected in the field, placing a limit on undetected objects of less than 43 mJy. There are no bright 2MASS sources within the IRAS error lobe of 14″of this star which could be responsible for IRAS confusion. These limits suggest it is highly likely that the excess detected at longer wavelengths is indeed centered on the star HD191089. Publicly available Spitzer IRS low resolution spectra (originally presented in Chen et al. 2006) is shown after photospheric subtraction on the SED of this object by a dashed line (see Figure 10). This spectra shows that at less than 12 μm there is no excess, which allows us to place limits on the minimum radius and maximum temperature of the dust around the star of no hotter than 110K (11.5AU, 0.″21) as fit by a blackbody curve (see Figure 10). The IRS data shows good agreement with the blackbody fit at longer wavelengths (20-40 μm), but a steeper cut-off at the short-wavelength end (8-15 μm), which may be an effect of grain properties such as chemical composition and size. The predicted size and flux level of this disk makes it an ideal candidate for imaging at 25 μm with an 8m telescope to determine the true size and nature of this disk.

The age of this source is subject to some uncertainty. Isochrone fitting has given an age of 3Gyr (Nordstrom et al. 2004) or 1.6Gyr (Chen et al. 2006). However using X-ray and lithium abundance data among other techniques, Zuckerman & Song (2004) put the age of this source at ≤ 100Myr. Moór et al. (2006) also suggested this source is a possible member of the β Pictoris moving group, giving HD191089 a likely age of 12Myr. As membership of this moving group is not yet confirmed, we have chosen to adopt an age of 100 Myr for this source. (The age of the system will have a bearing on the calculation of $f_{\rm max}$ described in section 6.2; note that a younger age would increase the value of $f_{\rm max}$ and so make the interpretation of this source's emission as possibly steady-state even stronger.)

HD12039: This star was identified by Hines et al. (2006) as having an excess at 24 μm of 7 mJy (3 σ detection) and no excess at 70 μm. The target aperture used in the Spitzer observations was 14.″7 at 24 μm. Further IRS spectra were taken with Spitzer, with a 0.″4 1 σ uncertainty radius in the spectrograph slit. This spectra shows the infrared emission departing from the photosphere at 12-14 μm (see Figure 4 of Hines et al. 2006).

HD12039 was studied with VISIR in the N band. At the N band this source is detected with S/N of 26, and calibrated flux of 77 ± 3 mJy; this is within 2 σ of the predicted photospheric emission. We place an upper limit on the excess at 11.85 μm of 14 mJy. No other source was detected within the field of view and we can place a limit of ≤ 2mJy on undetected sources. Our data agrees well with the Spitzer data in Hines et al. (2006); the Spitzer photometry limits excess to less than 32 mJy at 13 μm. The pointing accuracy achieved in the Spitzer observations, the lack of detection of additional sources within the field, and the agreement between the VISIR photometry and that of Spitzer suggests that the IRS spectra and MIPS photometry are indeed measuring an excess centered on the star.

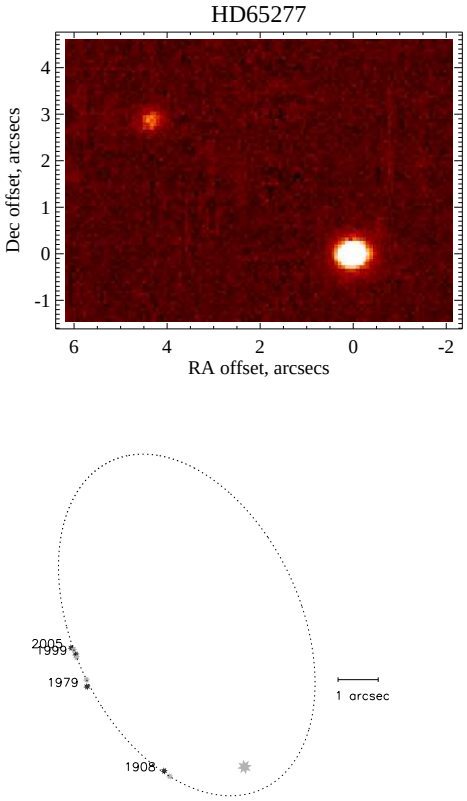

Fig. 11. The companion of HD65277 (images are North up, East left). Top: The N band VLT image of HD65277 and its binary companion offset by 5.″2 at position angle 56° East of North. Bottom: A fit to the orbit of this companion, with the VLT data shown as 2005. Black star symbols represent measured offsets and grey symbols the position of the companion predicted by the orbital fit. HD65277 is shown by the large light grey star symbol. See text for full details of the orbit.

SED fitting to the MIPS detections suggests a dust temperature of 120K, corresponding to an offset of 5AU (0.″12) from the star (see Table 3 and Figure 10, right for SED). This is in good agreement with a model for the emission proposed by Hines et al., which adopts blackbody grains at 4-6AU from the star. However, as pointed out in Hines et al. (2006), an alternative model of a power-law distribution of grains with radii between 0.4-1000μm located between 28 and 40 AU from the star provides an equally good fit to the data.

5.4. No dust detection

We now consider the members of the sample which were erroneously identified as having excess emission. Five of these objects have companion or background sources which are responsible for the IRAS detection of excess; one shows no evidence for current excess emission.

HD65277: This star has a 25μm excess at the 2.8 σ level, and no significant excess at 12 μm (see Table 1). In the 2MASS catalogue there is an additional object 2MASS 07575807-0048491 (which for brevity in the following discussion shall be referred to as HD65277b) at a separation of ∼5″ .

The primary object is detected at 182 ± 3 mJy and 78 ± 14 mJy in N and Q on VISIR. HD65277b is detected in the M and N band images of TIMMI2 at 5 σ and 3 σ respectively. It is strongly detected in N by VISIR, with a calibrated flux of 32 ± 4 mJy and is detected at Q at the 3 σ level (14 ± 6 mJy including calibration errors, see Table 2). The N band VISIR image is shown in Figure 11. The companion is at Δra = 4.″32 ± 0.″09, Δdec = 2.″91 ± 0.″085. The observations place constraints on additional undetected objects within the VISIR field of view of 2 and 10 mJy at 12 and 18 μm respectively.

The measured levels of flux for the primary are consistent with the expected photospheric emission (see Figure 12, top left). We use the K band magnitude of the secondary as listed in the 2MASS catalogue and assume a common distance of 17.5 pc with the primary to fit the spectral type of the companion as M4.5. Note that this spectral type was found to be the best fit to the currently available data but remains subject to great uncertainty. The model profile is designed to be representative of the possible SED of the source only. The profile is modelled with a NextGen model atmosphere appropriate to this spectral type (Hauschildt, Allard & Baron 1999). The M band detection of the secondary is calibrated to the expected flux of the primary photosphere and is measured as 133 ± 25 mJy, a little low compared to the expected 244 mJy which may be the result of a large filter width ($\Delta\lambda$ = .69μm) and the TiO absorption features seen in M-type stars at around this wavelength. The VLT N band flux of HD65277b is also a little low, but scaling to the expected primary flux the difference is not significant above the 4 σ level.

Additional data available for this object allows us to make a preliminary estimate of the orbit for HD65277b. This orbit is shown in Figure 11. The VISIR data is the point marked as 2005 (exact epoch 2005.935). The data from 1999 is the 2MASS catalogue data (observed 12-01-1999). The earlier data are listed in the Washington Double Star Catalogue (Worley & Douglass 1997). The orbital fit has the following parameters: $a = 95AU; e = 0.85; I = 35°; \bar{\omega} = 290°; \Omega = 100°$; with the last pericenter pass in 1885. The masses of the stars are taken to be 0.69 $M_\odot$ for the primary and 0.23 $M_\odot$ for HD65277b, as appropriate to their spectral types. The predicted flux of the binary at 25 μm is 12 mJy, and subtracting this from the IRAS measurements leaves an excess of only 59 ± 29 mJy, an insignificant detection. Thus we conclude that the IRAS detection of excess is caused by inclusion of the binary and is not indicative of circumstellar disk emission.

HD53246: This star has an excess at 12 μm of 293 mJy at the 9.8 σ level, and at 24 μm of 143 mJy at the 5.5 σ level (Table 1) based on the IRAS catalogue. This star is detected in the MSX catalogue at 8.28μm, with flux 164 ± 19 mJy. This detection is consistent with the expected photosphere at this wavelength (168 mJy).

In the observations presented here a source is detected within 1″of the expected source location at a signal/noise of 4.5, but calibration errors introduce high uncertainty in the photometry. The calibrated flux is 111 ± 30 mJy (expected photospheric emission from HD 53246 is 87 mJy). However there is no evidence for excess as the fluxes are in line with that expected from the photosphere, and limit any undetected excess to less than 114mJy (see Figure 12, top right, for SED). The possibility of a companion within the TIMMI2 field of view of above 62 mJy is ruled out at the 3 σ level.

We attribute the significant excess emission to an additional MSX source (G234.4643-07.5741) at 89 ″(position angle -11°) detected at 8.28μm at a level of 179 ± 19 mJy. The IRAS Point Source Catalogue position for this object is between HD53246 and the MSX source, offset from HD53246 by 31″ at a position angle of 94°. The error ellipse given in the catalogue is 44″ by 10″ (with position angle 101). This is larger than average for the IRAS catalogue (estimated to be 16″ in the cross-scan direction and 3″ in the in-scan direction, Beichman et al. 1988), suggesting that the IRAS fluxes could be contaminated by emission falling outside the TIMMI2 field of view. We believe that confusion caused by the nearby MSX source is the likely origin for the excess. This MSX source has a very similar level of emission to the star, with a flux of 170 ± 19 mJy at 8.6 μm compared to HD53246 with a flux of 164 mJy, but no other published detections and so a spectral type cannot be ascribed. As the star is in the galactic plane ($b = -7.6°$), it is likely to be a background source. Assuming the same flux as the star at the IRAS wavelengths reduces the excess emission to 165 mJy and 114 mJy at 12 and 25 μm respectively, with significance of 5.5 and 4.4 σ respectively, however the additional uncertainty of having no information on the MSX source and thus only estimated emission at the IRAS wavelengths means it is quite possible that the MSX source has higher flux at the IRAS wavelengths and thus we cannot view the IRAS photometry as evidence of excess emission.

HD79873: HD79873 has a marginally significant excess at 25 μm but no significant excess at shorter or longer wavelengths. The 25 μm excess was 71 mJy at just below the 2 σ level (Table 1). This star also has a companion with V band magnitude of 11 in the Visual Double Star catalogue at a separation of 2.″1. (The primary has a corresponding Vmag of 6.5.) It is not resolved in 2MASS.

The primary is detected in the TIMMI2 and VISIR observations at N and Q, and find levels of emission consistent with the expected photospheric emission (160 ± 18 mJy and 39 ± 9 mJy at N and Q, expecting 167 and 65 mJy from photosphere, see Table 3). The star was also observed in the M band filter of TIMMI2, in which the secondary was detected at the 2.6 σ level. The object is offset by 2.″55 ± 0.″25 at position angle -28 ±6°. The flux ratio of the primary to the secondary at M is 191 ± 20. The N band detection at the location of the secondary is not significant, at only 1.5 σ, and the flux limits shown on the SED of the binary object (in Figure 12, binary plotted with dashed line and limits with open circles) are those scaled to the photosphere of the primary using the ratio of fluxes. In the Q band we find no detection of this object, and place a limit on its emission accordingly. The V band magnitude of the binary object and the assumption that the object is at the same distance as the primary (68.9 pc) are used to fit the spectral type as K5.

The photometry of the primary is consistent with photospheric emission only. The IRAS excess is at the limits of significance, and once the secondary emission is taken into account the excess falls to 68 ± 39 mJy, a non-significant level.

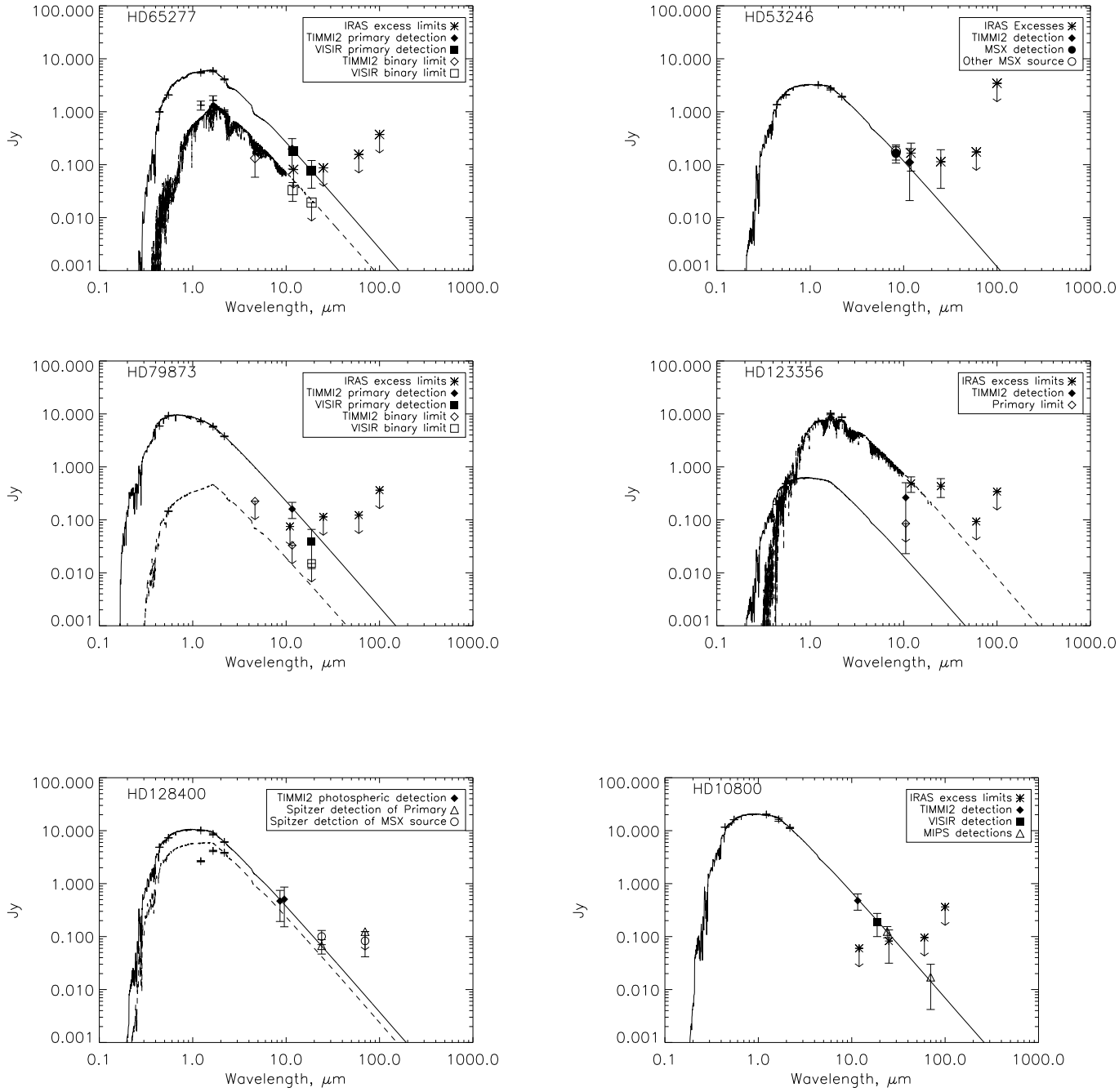

Fig. 12. The SED fits and limits for objects without confirmed hot dust. Photospheric emission as modelled by Kurucz atmospheres are shown as a solid line. Dashed lines are the photospheric models of the binary (modelled occasionally using NextGen spectra - see text). Errors are 3 sigma, and upper limits are also 3 sigma.

Thus we attribute the excess detected in the IRAS observations to the inclusion of the secondary object in the beam.

HD123356: Detections in the IRAS database of the star HD123356 suggest this object has excess emission at 12 and 25 μm of 1270 and 615 mJy respectively (detections of excess are 24 and 11 σ respectively, Table 1). This star has an additional object within 2.″5 identified in the WDS and 2MASS catalogues (2MASS 14073401-2104376, for brevity this shall be called HD123356b in the following discussion). HD123356b is far brighter in the J, H and K bands (taken from the 2MASS database), although it is fainter in the visual than HD123356 (12.2mag compared to 10mag). Sylvester & Mannings (2000) observed HD123356 at UKIRT using a low resolution spectrometer. The aperture used for the UKIRT spectroscopy is 5.″5,

meaning that the companion object is at the edge of the measured region. They found around half the level of flux that was expected from the IRAS detections. The authors suggested that all the excess emission may be centered on H123356b.

This source was observed at 10.54 μm only, and an object detected at 207 ± 78 mJy (S/N on source excluding calibration uncertainties is 3.2). As this object could not be acquired at M due to saturation of the filter, the pointing accuracy is reduced to 5-10″ here and so it cannot be confirmed which object was detected. A limit of 164 mJy can be placed on any undetected sources within the field of view.

Given the expected flux from HD123356b from extrapolation of the 2MASS observations is 681 mJy it is extremely likely that we observed the secondary source HD123356b. The limit placed on undetected objects in this observation is consistent with the non-detection of the primary. We show the SED of these two objects in Figure 12, with an M5 NextGen model atmosphere shown as a representative fit to the secondary, although with so little information available on HD123356b an identification of its nature cannot be made. The confusion created by the presence of this object is however the likely source of the IRAS excesses since although subtracting the M star fit to HD123356b does not account for all the IRAS flux, it is likely this source could be a reddened background object and so have higher infrared flux than is suggested by the M star profile. Otherwise the excess emission of HD123356 would have to be $L_{IR}/L_* = 0.17$, far brighter than any known debris disk source.

HD128400: HD128400 has an IRAS excess at above 7 σ at 12 μm of 178 mJy (Table 1). Gaidos (1999) suggests an age of 300Myr based on the star's likely membership of the Ursa Major moving group.

Poor conditions meant that photometry could not be performed from the TIMMI2 observations of this object. The star was at 469 ± 41 (92) mJy and 507 ± 61 (118) mJy at 8.6 and 9.56 μm respectively (parentheses indicate inclusion of calibration error). We detected no additional sources within the 64″ x 48″ field of view of the TIMMI2 instrument. This limits undetected background objects to less than 109 mJy at 8.6 μm. However, there is an additional object in the 2MASS catalogue at 83″ (2MASS 14421386 - 7508356, in the following discussion this object shall be called HD128400b for brevity). The source listed in the IRAS Point Source Catalogue is at a distance of 23″ from HD128400. Pointing errors for this observation are listed as 28″ in major axis, 9″ in minor axis, with the major axis at position angle 117°. The 2MASS source is at a position angle of nearly 99°, almost exactly along the axis of greatest error.

Publicly available Spitzer data analysed using the MOPEX package (Makovoz and Marleau, 2005; Makovoz and Khan, 2005) indicates that HD128400b emits at a similar level to HD128400 at 24 μm, with the primary having a flux of 55 ± 6 mJy and HD128400b a flux of 87 ± 9 mJy. At 70 μm the secondary is detected at a level of 35 ± 5 mJy, but HD128400 itself is not detected giving an upper limit of 14 mJy. The emission spectra of HD128400b at $\leq$ 24μm is best fitted by a spectral type of M7, implying that level of emission from HD128400b at 70 microns is much higher than expected (predicted < 1 mJy) and so presumably has its own excess. If the source was a main sequence star it would be at 3 pc, making it a truly remarkable object. However given that it is close to the galactic plane ($b = -13°$) we conclude that it is likely to be a reddened background object

Given the photometric results presented here, the longer wavelength Spitzer photometry and the size of the pointing error in the IRAS data, we believe that confusion with the 2MASS source is the cause for the excess identification of HD128400, as is confirmed by IRS spectra showing photospheric emission only at 12 μm (Beichman et al. 2008, in prep.).

HD10800: HD10800 was reported as having an excess at 25μm in the IRAS database of 82 mJy (4.5 σ detection, see Table 1). This source was observed with MIPS by Bryden et al. (2006) at 24 and 70 μm and no excess found, with a 3σ upper limit to excess of 33 and 16 mJy respectively.

Emission centered on the stellar location to within 1″of 477 ± 54 mJy at 11.59 μm and 186 ± 29 mJy at 18.72 μm is detected. The predicted stellar photosphere at these wavelengths is 513 and 200 mJy respectively, thus there is no evidence for excess emission in these observations which place upper limits on excess of less than 126 mJy at 11.56 μm, and less than 73 mJy at Q. The detections and those of Bryden et al. are shown on the SED plot (Figure 12). Furthermore the results can place limits on possible background sources of less than 14 mJy in the Q band (39 mJy in N); the IRAS excess is therefore not due to an unseen companion within a 19.″2 square of the source (field of view of VISIR). There are no bright 2MASS sources within the pointing errors of the IRAS observation likely to be the source of the additional IRAS flux (as for HD53246 or HD128400). Thus there is no evidence that this source currently has an associated excess. It is possible that this source has evolved in the terrestrial regions since the epoch of the IRAS observations, and so the emission has disappeared beyond the detection limits of these observations. Alternatively it may be that this object is a statistical anomaly, as the detection of excess from the IRAS catalogue is at only a moderately significant level.

6. Discussion

6.1. Results summary

6.1.1. Hosts of mid-infrared excess

In this study we have confirmed the presence of warm dust around three stars, η Corvi, HD145263 and HD202406. The last two of these sources are young, around a few million years old, and may be still forming planetary systems, although it is notable that these sources have relatively low L_{IR}/L_* compared to typical T Tauri stars (Padgett et al. 2006) and so these may be transitory objects (transitioning between proto-planetary and debris disk stages). η Corvi, on the other hand, is around 1.3 Gyr old, at an age where we would expect any planetary system to have finished forming (see e.g. de Pater and Lissauer, 2001). For three other sources we have placed stringent limits on the possible level of any background/companion object within the

fields of view of the instruments. From these limits and the photometry of the IRAS catalogue and published Spitzer data, we have concluded that the excesses in the mid-infrared, originally determined from the IRAS catalogue, are highly likely to be centered on the stars for HD12039, HD69830, and HD191089.

6.1.2. Background exclusion and the importance of confirmation

Five of the sources in the sample turned out to be the result of source confusion in the IRAS beam. For HD65277, HD79873 and HD123356 the source could be identified in the TIMMI2 and VISIR images (albeit without a detection of the primary in the case of HD123356). For HD53246 and HD128400, the source responsible for the excess measured in analysis of the IRAS catalogue was $\sim 80''$ away, and so beyond the field of view of TIMMI2. These examples show the dangers of trusting the IRAS catalogue without full and detailed analysis of all pertinent catalogue data and follow-up observations. Indeed out of an initial sample of 11 sources believed to be hosts of mid-infrared excess, only 3 were confirmed in this study, and a further 2 by other authors.

HD10800 was shown to have no excess and no other source which is likely to be responsible for the levels of the IRAS detections. The significance of the excess as judged from the IRAS measurements is not high, at 4.5 σ. Thus it is possible that this object never had an excess and is an illustration of the potential errors to be found when searching close to the significance limit for excess (Song et al. 2002).

The need for confirmation of debris disk candidates has also been found by Rhee et al. (2007), who combined data from the IRAS database, the Hipparcos catalogue and the 2MASS catalogue to search for excess sources, finding a total of 153 sources. Included in this paper are 97 sources rejected for reasons including contamination by additional sources or cirrus, pointing inaccuracy of the IRAS measurements, and follow-up with Spitzer showing photospheric emission only. Additional source contamination is a particular issue for sources in the galactic plane. In this study HD53246 and HD128400 are in and near the galactic plane respectively, and have been found to have been erroneously identified as hosts of debris. HD155826, identified by Lisse et al. (2002) as being a bogus disk due to source confusion also lies in the galactic plane at $b = -0.1$. Removal of bogus disks is important when attempting to perform a statistical analysis on disk populations. Greaves and Wyatt (2003) include HD128400 as a disk host. Removing this disk changes their statistics from 4/22 to 3/22 young G stars hosting a disk (a total of 11/177 G star systems possess a disk as opposed to their quoted 12/177). Though this is only the removal of a single disk the sample size involved is not particularly large, and so the removal of only a few sources can be significant and the additional uncertainty from bogus disks should be born in mind when considering statistical studies (such as analysing disk evolution over time or dependence on stellar spectral type or environment) needing large samples. Fortunately the Spitzer Space Telescope has greater resolution (as illustrated by HD128400) and is now providing more reliable large disk samples (see e.g. Meyer et al. 2006).

6.1.3. Extension limits

Our new methods of testing extension limits have quantified how for small disks the variation and subsequent uncertainty in the PSF will provide the greatest restrictions in the ability to detect the disk extension in a particular observation whereas for large disks detection is limited by the S/N that can be achieved on the disk (which has decreasing surface brightness with increased angular size). The optimal size of a disk to be detected (i.e. the disk size requiring the least bright disk to be detected as an extended source) is one with a radius approximately equal to the FWHM of the PSF (for disks at 18 μm the FWHM on an 8m telescope $\simeq 0\farcs6$ which translates to a disk offset of 12 AU for a systems at 20pc).

Analysis of the observations presented in this paper including: comparison of FWHM fits to image profiles; analysis of surface brightness profiles; and simple subtractions of PSFs (determined from standard star observations) from science images and examination of the residuals, has revealed no evidence for extension around any of the observed objects. A new technique of extension limits testing can give quantifiable constraints on which disk models can be ruled out and at what level of certainty with such data. The extension testing limits have been used to constrain the possible disk populations of η Corvi (see section 5.1). The limits suggest that model A, in which the mid-infrared emission comes from a single temperature component is more likely at a 2.6 σ level, however a deeper Q band image should either resolve or rule out the mid-temperature ($\sim$ 120K) component of model B (the three temperature fit), as described in detail in section 5.1. The hot components of both dust models (at $0\farcs09$ and $0\farcs07$ for models A and B respectively) are comparable to the pixel scales of the detectors of VISIR and MICHELLE ($0\farcs075$ and $0\farcs099$ respectively). Disks on these scales cannot be resolved using these single aperture 8m instruments (see 5.1 for further discussion), and will require the resolving power of an interferometer to be resolved.

This extension testing method can be applied to future observations of these and other potential disk sources to determine what limits can be placed on unresolved disks. Furthermore, the predictions of this modelling, as shown in section 3.2.3, can be used to determine which sources, with predicted disk flux and radii, will be the most fruitful sources for imaging with single large-aperture telescopes. Work exploring this exciting aspect of the technique is underway and the results shall be presented in a forthcoming paper (Smith and Wyatt, in prep.). For now we note that this technique provides more quantitative limits on the location of dust, and note that the possibility of detecting extended emission is strongly affected by whether the dust is confined to a single radius (temperature) or in a more broad distribution with multiple temperatures.

6.2. The nature of mid-infrared excess sources

Four recent papers have looked at the statistics of mid-infrared excess around Sun-like stars: Gaidos (1999); Laureijs et al. (2002); Hines et al. (2006); and Bryden et al. (2006). All of these surveys found hot emission to occur around 2±2% of FGK-type stars, with Trilling et al. (2008) finding 24 μm excess around $4\ ^{+2}_{-1.1}$% of Sun-like stars observed with Spitzer, although it is worth noting that these surveys are limited by their photometric accuracy and therefore there may be a larger population of hot disks that are more tenuous and thus have a fractional luminosity below the current levels of detectability in these surveys. The sample of objects in the study presented in this paper were chosen deliberately to be the objects thought to have excess following analysis of the IRAS catalogue results, and so does not represent an unbiased sample. Our detection rate cannot be compared with these statistical results. For any star observed in the survey papers mentioned above and included in this paper the conclusions regarding the presence of excess emission are the in agreement with the exception of HD128400, which was included in the work by Gaidos (1999) as a positive detection of excess. As shown in section 5.4, the results show no evidence for excess, and a nearby 2MASS source is likely to be the source of confusion in the IRAS results. This result does not change the validity of the 2±2% statistic however, as for Gaidos (1999) it reduces the detected excesses to 0/36 (giving a hot emission occurrence of 0±3% from this paper alone).

Many disks have been observed around T Tauri and Herbig Ae/Be stars (see e.g. Meeus et al. 2000). Massive protoplanetary disks have been observed around stars up to 10Myr (see e.g. Meyer et al. 2007), at which point the disks rapidly disappear to leave at best a low fractional luminosity dust belt. The disks of HD145263 and HD202406 lie at an intermediate evolutionary stage, having ages of 9 and 2 Myr respectively, and exhibit a relatively high fractional excess (see Table 3) for debris disks, but these values are low compared to disks around typical T Tauri stars (Padgett et al. 2006). Recent work with Spitzer on clusters of similar ages to these two sources have indicated that mid-infrared excess emission may be the result of planet building processes in the terrestrial region (see e.g. Currie et al. 2007). Fitting the excess emission of HD145263 and HD202406 with a blackbody suggests that the dust lies in the terrestrial region, even with a 3 times underestimate of the dust location for HD145263 (see table 3). It is therefore possible that the dust is the result of planet building and not the evolution of a small Kuiper belt. Further studies of these sources may help to elucidate their nature.

Analytical modelling by Wyatt et al. (2007) has demonstrated that there exists a maximum fractional excess which can be expected from a belt of planetesimals in a steady-state collisional cascade. This is because more massive disks which could potentially produce more emitting dust grains process themselves more quickly. The equation given for this prediction is $f_{\rm max} = L_{\rm IR}/L_* = 0.16 \times 10^{-3} r^{7/3} t_{age}^{-1}$. The application of this model to the stars with confirmed infrared excess is shown in the last column of Table 3. Within the uncertainties of this model, a disk with $f_{\rm IR} > 1000\, f_{\rm max}$ is unlikely to be evolving in a steady state collisional cascade. Within these limits, HD145263 and HD202406 could be steady-state disks given their young ages. Their fractional excesses are high compared to typical debris disks however and it is possible these disks are in a transitional phase from proto-planetary to debris disk (see e.g. Calvet et al. 2005). As shown in Wyatt et al. (2007), HD69830 and η Corvi (assuming the simple single mid-infrared component, see later in this section) have excess emission at a much higher level than would be expected for collisionally evolving disks given their age and radius, and thus it is expected that there is a transient source for some of the emitting material.

There have been several suggested sources of transient emission put forward in the literature. One possible source of this emission would be the recent collisional destruction of two (or more) massive bodies (Song et al. 2005). In our own asteroid belt a collision large enough to more than double the emission from the belt occurs approximately every 20 million years (Durda and Dermott 1997). The recent analytical modelling of Wyatt et al. (2007) has shown that for the systems with disks that are assumed to be transient ($f_{obs}/f_{max} >> 1000$) the single massive collision hypothesis is highly unlikely to be able to account for such a massive excess. It may be that these systems have recently undergone some dynamical stirring (orbital migration of a massive planet, recent stellar fly-by etc.) that has triggered a Late Heavy Bombardment-like period (Gomes et al. 2005). The Late Heavy Bombardment was a period approximately 3.8-4 Gyr ago when the inner planets of the solar system experienced a greatly enhanced rate of asteroidal collision, possibly due to the orbital migration of Jupiter. The extreme excess emission found around BD+20 307 (a star possessing mid-infrared excess not included in this study's sample) is thought to have come from the excitation of a belt resulting in massive or frequent collisions (Song et al. 2005). As noted by these authors, this system has an extremely high fractional excess and would therefore be in an extreme state of collisional destruction. The recent sublimation of a massive comet would also produce a transient peak in infrared excess. Beichman et al. (2005) have performed spectroscopy of the HD69830 system. The resulting spectra showed marked similarities to the emission spectra of the Hale-Bopp comet, with several peaks of crystalline olivine identified. Further work by Lisse et al. (2007) has shown that the spectra is more similar to that of a disrupted P or D-type asteroid. Spectral analysis may be the most useful tool to analyse the possibility of cometary sublimation or asteroid disruption for such systems.

However, the transient interpretation is highly dependent on the radial location of the dust as can be seen in the above equation for f_{max}, ($f_{max} \propto r^{7/3}$). In fitting the photometric results of excess emission we have made assumptions of grains emitting as blackbodies at a single temperature. Such an assumption may lead to an underestimation of disk size by up to a factor of three, as emitting grains are typically small and hotter than blackbody (see e.g. Schneider et al. 2006). Further a more extended dust distribution could lead to an over-estimation of the disk size by assuming a single size and temperature for the emitting grains. The uncertainty remaining in the SED fits of these objects can only be avoided by direct observational con-

firmation of the size of the emitting region. The example of η Corvi is an appropriate illustration of this issue. In model A the mid-infrared emission cannot be explained by a steady-state evolution (see discussion above and Table 3). In model B the hot dust component at 360K is also likely to be transient, however the mid-temperature component at 120K (12 AU) can be explained by a collisionally evolving disk at 12 AU (Table 3). Indeed this population of dust lies in an appropriate location to be a possible parent planetesimal belt to the hot dust emission according to Figure 4 of Wyatt et al. (2007). This would require a radial transport mechanism that would move the dust from the 12 AU belt to a 1.3 AU location, which is not well modelled or understood, but could be analogous to the inward scattering of planetesimal material into the terrestrial regions during the Late Heavy Bombardment period initiated by the resonance crossing of Jupiter and Saturn (see Wyatt et al 2007 discussion for elaboration on this scenario). Thus the model with a total of three components (model B) could represent two steady state populations (the 12 AU mid-infrared component and the large sub-mm disk) and a transient component, the source of which is currently unknown. This model is ruled out by current data at the 2.6σ level, although it is important to note that whichever model we adopt for η Corvi there is a transient component, and so we are unlikely to find a fit to this system which does not require some transitory contribution to the excess emission. However, as highlighted in this study, a confirmed radial location is key to understanding the nature of this system, and the hot dust populations as a whole.

7. Conclusions

We have presented an observing programme focussing on main sequence F, G and K stars purported to have infrared excess. The findings can be summarised as follows:

- We have confirmed the excess emission to be both real and centred on the star for 3 objects, all of which have excess emission within the terrestrial regions as fitted by SED modelling. Two of these objects are believed to be pre-main sequence stars.
- For 5 further objects, the dust was found to be from a companion/background source, and not associated with the star. This demonstrates the importance of high resolution imaging as a tool to confirm IRAS sources.
- One object was found to have no associated excess nor any object nearby likely to be responsible for the levels of flux in the IRAS measurements.
- Our new method of testing extension limits has enabled us to place limits on the radial extent of some disk populations and shown that for some others, single aperture imaging with current 8m-class telescopes will not be able to resolve the extent of the disk.
- The extension limits testing suggests a fit to the η Corvi emission spectrum using a single mid-infrared component at around 320K and a cool component at 40K is more likely to represent the true dust distribution than a fit using two mid-infrared components at 360K and 120K, together with the cool 40K dust at the 2.6 σ level (or lower or higher significance depending on the geometry of the dust belts).

Sources of hot dust emission fall into distinct groupings. Either the sources are young and possibly transitional, in which case the dust can be primordial, or the result of steady-state evolution (e.g. HD145263 and HD202406), or they are old and sources of transient emission (η Corvi and HD69380), or they are old and have relatively low radius steady-state planetesimal belt (HD12039 and HD191089, and possibly the mid-temperature component of η Corvi).

The rare hot dust in main sequence systems may be transient as suggested by comparison to collisional modelling. However, uncertainties inherent from the SED modelling process mean that only by resolving the location of the emitting region can we deprive these systems of their enigmatic status. Our new method of extension testing allows us to constrain dust locations much more tightly than a simple comparison with the PSF. Application of these techniques to further observations and other sources is one way to determine the radial extent of the dust emission and thus begin to determine the nature of these hot dust sources.

Acknowledgements. RS is grateful for the support of a PPARC studentship. MCW is grateful for the support of a Royal Society University Fellowship. The authors are grateful to Ben Zuckerman for directing our attention to the Spitzer observations of HD128400, and to Geoff Bryden for fruitful discussions on these observations. Furthermore the authors wish to extend their thanks to Christine Chen for providing the IRS spectra of η Corvi, and to Chas Beichman for the spectra of HD69830. Based on observations made with ESO Telescopes at the La Silla and Paranal Observatories under programme IDs 71.C-0312, 72.C-0041 and 74.C-0700. Also based on observations obtained at the Gemini Observatory, which is operated by the Association of Universities for Research in Astronomy, Inc., under a cooperative agreement with the NSF on behalf of the Gemini partnership: the National Science Foundation (United States), the Particle Physics and Astronomy Research Council (United Kingdom), the National Research Council (Canada), CONICYT (Chile), the Australian Research Council (Australia), CNPq (Brazil) and CONICET (Argentina).

References

Absil O., di Folco E., Mèrand A., et al., 2006, A&A, 452, 237
Backman D.E. & Paresce F., 1993, in Protostars and Planets III, eds. E. H. Levy & J. I. Lunine (Tucson: University Arizona Press), 1253
Barrado y Navascués D., Stauffer J.R., Song I., & Caillault J.-P., 1999, ApJ, 520, L123
Beichman C.A., Neugebauer G., Habing H.J., Clegg P.E., & Chester T.J., 1988, in Infrared Astronomy Satellite (IRAS) Catalogs and Atlases, Volume 1, Explanatory Supplement, NASA
Beichman C.A., Bryden G., Gautier T.N., et al., 2005, ApJ, 626, 1061
Bryden G., Beichman C.A., Rieke G.H, et al., 2006, ApJ, 636, 1098
Calvet N., D'Alessio P., Watson D.M., et al., 2005, ApJ, 630, L185
Chen C.H., Sargent B.A., Bohac C., et al., 2006, ApJS, 166, 351
Cohen M., Walker, R.G., Carter B., et al., 1999, AJ, 117, 1864
Currie, T., Kenyon S.J., Balog Z., et al., 2007, ApJ, 672, 558
de Pater I., & Lissauer J.J., 2001, Planetary Sciences, (Cambridge: Cambridge University Press)
Dermott S.F., Jayaraman S., Xu Y.L., Gustafson B.A.S., & Liouet J.C., 1994, Nature, 369, 719

Dermott S.F., Durda D.D., Grogan K., & Nesvorny D., 2002, in Proceedings if Asteroids, Comets, Meteors - ACM 2002, ed. B. Warmbein, (Noordwijk, Netherlands: ESA Publications Division), 319
Di Folco E., Absil O., Augereau J.-C., Mérand A., Coudé du Foresto V., et al., 2007, A&A, 475, 243
Durda D.D. and Dermott S.F., 1997, Icarus, 130, 140
Franco G.A.P., 1989, A&A, 223, 313
Gaidos E.J., 1999, ApJ, 510, L131
Gomes R., Levison H.F., Tsiganis K., & Morbidelli A., 2005, Nature, 435, 466
Greaves J.S., & Wyatt M.C., 2003, MNRAS, 345, 1212
Greaves J.S., Holland, W.S., Wyatt M.C., et al., 2005, ApJ, 619, L187
Hauschildt P.H., Allard F., & Baron E., 1999, ApJ, 512, 377
Hines D.C., Backman D.E., Bouwman J., et al., 2006, ApJ, 638, 1070
Holland W.S., Greaves J.S., Zuckerman B., et al., 1998, Nature, 392, 788
Hollenbach D.J., Yorke H.W., & Johnstone D., 2000, in Protostars and Planets IV, eds Mannings V., Boss A.P. and Russell S.S., University of Arizona Press, 401.
Honda M., Kataza H., Okamoto Y.K., et al., 2004, ApJ, 610, L49
Jura M., 2004, ApJ, 603, 729
Kalas P., Graham J.R., Beckwith S.V.W., Jewitt D.C., and Lloyd J.P., 2002, ApJ, 567, 999
Kalas P., Fitzgerald M.P., and Graham J.R., 2007, ApJ, 661, L85
Kenyon S.J., and Bromley B.C., 2002, ApJ, 577, L35
Lagage P.O., and Pantin E., 1994, Nature, 369, 628
Larwood J.D., and Kalas P., 2001, MNRAS, 323, 402
Laureijis R.J., 2002, A&A, 387, 285
Lisse C.M., Schultz A., Fernandez Y., et al., 2002, ApJ, 570, 779
Lisse C.M., Beichman C.A., Bryden G. and Wyatt M.C., 2007, ApJ, 658, 584
Lovis, C., Mayor, M., Pepe F., et al., 2006, Nature, 441, 305
Mannings V. and Barlow M.J., 1998, ApJ, 497, 330
Makovoz D. and Khan I., 2005, in ASP Conf. Ser. 132, Astronomical Data Analysis Software and Systems VI, ed. P. L. Shopbell, M. C. Britton, & R. Ebert (San Francisco: ASP)
Makovoz D., and Marleau F.R., 2005, PASP, 117, 1113
Matthews B.C., Kalas P.G, & Wyatt M.C., 2007, ApJ, 663, 1103
Meeus G., Waters L.B.F.M., Bouwman J., et al., 2001, A&A, 365, 476
Meyer M.R., Hillenbrand L.A., Backman D., et al., 2006, PASP, 118, 1690
Meyer M.R., Backman D.E., Weinberger A. & Wyatt M.C., 2006, in Protostars and Planets V, eds. Reipurth B., Jewitt D. & Keil K., (Tuscan: University Arizona Press)
Moór A., Ábrahám P., Derekas A., et al., 2006, ApJ, 644, 525
Moran S.M., Kuchner M.J., & Holman M.J., 2004, ApJ, 612, 1163
Nordstrom B., Mayor M., Andersen J., et al., 2004, VIZIER On-line Data Catalog:*The Geneva-Copenhagen Survey*
Oudmaijer R.D., van der Veen W.E.C.J., Waters L.B.F.M., et al., 1992, A&AS 96, 625
Padgett D.L., Cieza L., Stapelfeldt K.R., et al., 2006, 645, 1283
Palla F., & Stahler S.W., 1993, ApJ, 418, 414
Ratzka Th., Leinert, Ch. Henning Th., et al., 2007, A&A, 471, 173
Rhee J.H., Song I., Zuckerman B., & McEwain M., 2007, ApJ, 660, 1556
Schneider G., Silverstone M.D., Hines D.C., et al., 2006, ApJ, 650, 414
Sheret I., Dent W.R.F., & Wyatt M.C., 2004, MNRAS, 348, 1282
Siess L., Dufour E., Forestini M., 2000, A&A 358, 593
Song I., Caillault J.-P., Barrado y Navascués D., Stauffer J.R., & Randich S., 2000, ApJ, 533, L41
Song I., Weinberger A.J., Becklin E.E., Zuckerman B., & Chen C., 2002, AJ, 124, 514
Song I., Zuckerman B., Weinberger A.J., & Becklin E.E., 2005, Nature, 436, 363
Stencel, R.E., & Backman, D.E., 1991, ApJS, 75, 905
Sylvester R.J. & Mannings V., 2000, MNRAS, 313, 73
Telesco C.M., Fisher R.S., Wyatt M.C., et al., 2005, Nature, 433, 133
Trilling D.E., Bryden G., Beichman C.A., et al., 2008, ApJ, in press, astro-ph/0710.5498
Valenti J.A., & Fischer D.A., 2005, ApJS, 156, 141
van den Ancker M.E., The, P.S., Tjin A Djie, H.R.E., et al., 1997, A&A, 324, L33
Wilner D.J., D'Alessio P., Calvet N., Claussen M.J., & Hartmann L., 2005, ApJ, 626, L109
Wyatt M.C., 2003, ApJ, 598, 1321
Worley C.E., & Douglass G.G., 1997, A&AS, 125, 523
Wyatt M.C. and Dent W.R.F., 2002, MNRAS, 334, 589
Wyatt M.C., Dermott S.F., Telesco C.M., et al., 1999, ApJ, 527, 918
Wyatt M.C., Greaves J.S., Dent W.R.F., & Coulson I.M., 2005, ApJ, 620, 492
Wyatt M.C., Smith R., Greaves J.S., et al., 2007, ApJ, 658, 569
Zuckerman B., 2001, ARA&A, 39, 549
Zuckerman B., and Song I., 2004, ApJ, 603, 738
Zuckerman B., Song I., Bessell M.S., Webb R., 2001, ApJ, 562, L87